To the Graduate Council:

I am submitting herewith a thesis written by Scott E. Lasley entitled "Investigation of the Threshold Behavior of the Cross Sectionfor Collisional Dissociation of Diatomic Molecules." I have examined the final copy of this thesis for form and content and recommend that it be accepted inpartial fulfillmnent of the requirements for the degree of Master of Science with a major in Physics.

Marianne Breinig
Marianne Breinig, Major Professor

We have read this thesis
and recommend its acceptance:

David Pegg

Stuart B. Elston

Accepted for the Council:

Vice Provost
and Dean of The Graduate School

STATEMENT OF PERMISSSION TO USE

In presenting this thesis in partial fulfillment of the requirements for a Master of Science degree at the University of Tennessee, Knoxville, I agree that the Library shall make it available to borrowers under rules of the Library. Brief quotations from this thesis are allowable without special permission, provided that accurate acknowledgement of the source is made.

Permission for extensive quotation from or reproduction of this thesis may be granted by my major professor, or in her absence, by the Head of Interlibrary Services when, in the opinion of either, the proposed use of the material is for scholarly purposes. Any copying or use of the material in this thesis without for financial gain shall not be allowed without my written permission.

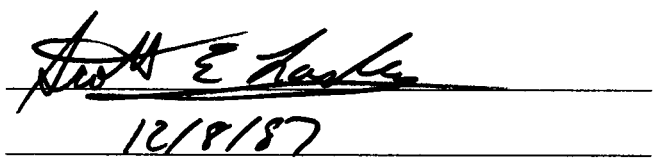

12/8/87

INVESTIGATION OF THE THRESHOLD BEHAVIOR OF THE CROSS SECTION FOR COLLISIONAL DISSOCIATION OF DIATOMIC MOLECULES

A Thesis

Presented for the

Master of Science

Degree

The University of Tennessee, Knoxville

Scott E. Lasley

March 1988

Acknowledgements

I would like to express my deepest appreciation for the guidance and assistance given to me by my adviser, Dr. Marianne Breinig. I would also like to thank my family, friends, and the members of the Atomic Physics Group at the University of Tennessee for their support. I would finally like to thank the faculty of the Space Physics Group at the University of Maryland for allowing me to complete this project while under their employ.

Abstract

The energy spectra of positive ions resulting from the dissociation of singly charged diatomic molecules after collisions with neutral gas targets were measured in coincidence with the neutral fragments. The yields near threshold were studied to determine if they obeyed a two-body threshold law.

N_2^+, H_2^+, and ArH^+ ions were created in an ion source and accelerated to energies between six and twenty keV. The ions collided with He and Xe gas targets and dissociated. Energy spectra of the positively charged fragments ejected in the forward and backward directions were taken with a 160° spherical sector electrostatic analyzer in coincidence with the neutral fragments detected in a charge state analyzer. The spectra were transformed from the laboratory frame to the projectile rest frame. The resulting yields were studied as a function of energy near threshold to determine if their behavior was consistent with the predictions of two-body threshold laws.

The data indicate that two-body threshold laws do describe the energy dependence of the dissociation cross section near threshold. The behavior of the cross section resembles that of the cross section for electron detachment from negative ions measured by other investigators.

Table of Contents

CHAPTER

I. INTRODUCTION AND THEORY 1

A. INTRODUCTION 1
B. MOLECULAR STRUCTURE AND DISSOCIATION 2
C. TWO-BODY THRESHOLD LAWS 15
D. THE EXPERIMENTS 20

II. APPARATUS AND EXPERIMENTAL METHOD 25

A. ION SOURCE AND ACCELERATOR 25
B. THE ELECTROSTATIC ANALYZER 28
C. THE CHARGE STATE ANALYZER 32
D. ELECTRONICS AND DATA ACQUISITION 35

III. DATA ANALYSIS AND RESULTS 40

A. TREATMENT OF THE RAW DATA 40
B. DATA ANALYSIS 43
C. RESULTS 50
D. DISCUSSION 60

LIST OF REFERENCES 65

VITA 68

List of Tables

Table 1. Energy dependence of the normalization factor, N, and the cross section, σ, for various long range interactions.....18

Table 2. Constants for the transmission function, f, of an abberation free spectrometer.....31

List of Figures

Figure 1. Energy levels for bonding and antibonding orbitals of H_2^+ 7

Figure 2. Electron densities for bonding and antibonding orbitals of H_2^+. 7

Figure 3. Dissociation via Frank-Condon transitions.....13

Figure 4. One and two dimensional energy spectra of protons resulting from the dissociation of 20 keV ArH^+ impacting on He. 22

Figure 5. The accelerator.....26

Figure 6. An exploded view of the ion source.....27

Figure 7. A 160° spherical sector analyzer.....29

Figure 8. The charge state analyzer.....34

Figure 9. A typical ADC spectrum showing the peak and background scaler window settings. 38

Figure 10. A schematic of the data acquisition electronics.....39

Figure 11. Relative detection efficiency of channel electron multipliers vs ion energy for protons and Ar^+ ions.....42

Figure 12. A coincidence spectrum measuredfor 10 keV ArH^+ impacting on Xe. 44

Figure 13. The partitioning of velocity space into shells and segments. 46

Figure 14. A plot of the product of v and $\sigma(E)$ vs E, where $\sigma(E)$ is calculated for $\frac{d\sigma}{dv} = \frac{1}{v^2}$. 50

Figure 15. The energy spectra measured in the laboratory frame for 10 keV ArH^+ projectile impacting on He and Xe targets.....51

Figure 16. Energy spectra measured in the laboratory frame for 20 keV ArH^+ impacting on He and Xe targets.....51

Figure 17. P(E), proportional to the dissociation cross section $\sigma(E)$, vs total CM energy E for 10 keV ArH^+ impacting on Xe. 53

Figure 18. P(E), proportional to the dissociation cross section $\sigma(E)$, vs total CM energy E for 10 keV ArH^+ impacting on Xe and He targets with laboratory acceptance angles of 0.025 rad and 0.036 rad.. 54

Figure 19. $P(E) \alpha \sigma(E)$ vs E for 10 and 20 keV ArH^+ impacting on a Xe target.. 55

Figure 20. The average P(E) for ArH^+ averaged over the forward and backward directions and the He and Xe targets. 56

Figure 21. P(E) vs E obtained using 30 and 20 steps in the deconvolution process. 57

Figure 22. $P(E) \alpha \sigma(E)$ vs E for 6 keV N_2^+ projectiles.....58

Figure 23. $P(E) \alpha \sigma(E)$ vs E for 6 keV H_2^+ projectiles.....60

Figure 24. Detached electron energy spectra for collisional detachment of electrons from H^- on Kr at 25 eV.....62

Figure 25. Total photodetachment cross section for K^-.....63

CHAPTER I

INTRODUCTION AND THEORY

A. Introduction

Molecular physics is a complex field. One important goal of researchers working in this field is to determine the exact nature of the interaction potential between molecular constituents. Many different methods have been used to obtain information about this interaction potential.[1] Threshold laws have been used in atomic physics to study long range interactions between particles.[2] In this work, the behavior of the dissociation cross section for diatomic molecular ions in fast collisions with gas targets near threshold is investigated to determine if its energy dependence can be described by a two-body threshold law. The dependence of the dissociation cross section on the total kinetic energy of the dissociation fragments is studied for 10 and 20 keV ArH^+ projectiles and 6 keV N_2^+ and H_2^+ projectiles colliding with neutral He and Xe targets. Dissociation of diatomic molecules has been the topic of much research in the past twenty years.[3,4,5] If threshold laws do apply to this process, they can be used to learn more about the nature of the long range interaction between the molecular fragments.

This thesis is divided into three chapters. The first chapter contains theoretical information about molecules and threshold laws and a brief description of the experiments. Chapter 2 details the equipment and methods used to collect the data. Chapter 3 contains a discussion of the methods used to analyze the data and a presentation of the

results of the experiments. The usefulness of the techniques employed in this investigation is discussed along with the conclusions drawn from the data regarding threshold behavior of the dissociation cross section.

B. Molecular Structure and Dissociation

The Hamiltonian describing a system of nuclei and electrons interacting through Coulomb interactions is

$$(1) \quad H = \sum_i \frac{p_i^2}{2m} + \sum_\alpha \frac{P_\alpha^2}{2M_\alpha} + V(R,r)$$

where

$$(2) \quad V(R,r) = \sum_{\alpha<\beta} \frac{Z_\alpha Z_\beta e^2}{R_{\alpha,\beta}} - \sum_{i,\alpha} \frac{Z_\alpha e^2}{R_{i,\alpha}} + \sum_{i<j} \frac{e^2}{r_{i,j}} .$$

Here, α and β refer to nuclei of mass M, charge Z, and momentum P at positions R, while i and j refer to electrons of mass m and momentum p at positions r. It is not possible to solve the wave equation corresponding to this Hamiltonian analytically for even the simplest molecular systems, so approximation methods must be used. One common approach is to use the Born-Oppenheimer approximation. This method uses the fact that the electrons can adjust their motion quasi-statically to small changes in the nuclear positions since they are much lighter than the nuclei. In this adiabatic approximation, the electronic and nuclear wave functions are solved for separately.

The Born-Oppenheimer approximation consists of five steps:[6]

i) Assume that the complete molecular wave function, $\Psi(R,r)$, is a product of an electronic wave function, $\psi(R,r)$, and a nuclear wave function, $v(R)$:

(3a) $\Psi(R,r) = \psi(R,r)v(R)$

(3b) $H\Psi(R,r) = E\Psi(R,r)$.

ii) Fix the nuclei at positions $R = R'$. The resulting electronic Hamiltonian does not contain the term for the kinetic energy of the nuclei, $P^2/2M$. As a result, it only operates on $v(R')$ in a trivial way. The electronic Hamiltonian is given by

$$(4) \quad H_e = \sum_i \frac{p_i^2}{2m} + V(R',r)$$

iii) Solve the electronic wave equation

$$(5) \quad H_e\psi(R',r)v(R') = E'(R')\psi(R',r)v(R').$$

After dividing out the nuclear wave function the problem becomes one of finding the electronic wave function $\psi(R',r)$ with energy eigenvalues $E'(R')$. In principle, it is possible to solve this equation for a large number of different nuclear positions to determine the dependence of ψ and E' on R' and r.

iv) Substitute the product wave function Ψ into the complete Hamiltonian

$$(6) \quad \left[\sum_i \frac{p_i^2}{2m} + \sum_\alpha \frac{p_\alpha^2}{2M_\alpha} + V(R,r)\right]\psi(R,r)v(R) = E\psi(R,r)v(R)$$

v) Apply the adiabatic approximation

$$(7) \quad \frac{p_\alpha^2}{2M_\alpha}\psi(R,r)v(R) \approx \psi(R,r)\frac{p_\alpha^2}{2M_\alpha}v(R)$$

Using this approximation allows the electronic wave function to be factored out of the first term of the complete Hamiltonian, leaving

$$(8)\quad \psi(R,r)\sum_{\alpha}\frac{p_{\alpha}^{2}}{2M_{\alpha}}v(R) + \left[\sum_{i}\frac{p_{i}^{2}}{2m} + V(R,r)\right]\psi(R,r)v(R) = \varepsilon\psi(R,r)v(R),$$

where ε is an approximation to the true energy E. The term in brackets is equal to the electronic Hamiltonian H_e, and from equation 5, $H_e\psi(R,r)v(R) = E'\psi(R,r)v(R)$. With these substitutions, the equation for the nuclear wave function becomes

$$(9)\quad \psi(R,r)\left[\sum_{\alpha}\frac{p_{\alpha}^{2}}{2M_{\alpha}} + E'(R)\right]v(R) = \psi(R,r)\varepsilon v(R).$$

It can be shown by variational means that ε is a lower bound of the true energy.[6] The electronic wave function $\psi(R,r)$ can be divided out of both sides, leaving a wave equation for the nuclear motion $v(R)$. Equation 9 indicates that the nuclear wave function is solved in an effective potential $E'(R)$ which arises from the solution of the electronic wave equation with the nuclei held fixed.

The discussion of the electronic and nuclear states will be limited to the case of diatomic molecules. In the case of H_2^+, the simplest homonuclear molecule consisting of two protons and one electron, the electronic wave equation can be solved exactly by transforming to prolate spheroidal coordinates.[7] A different approach will be taken here, known as the method of linear combinations of atomic

orbitals (LCAO).[8] The LCAO approximation can be generalized to treat molecules that are more complex than H_2^+.

For internuclear distances much greater than the orbital radius of the electron about either proton, the electronic wave function will approximately be given by a hydrogenic wave function centered on either proton. A linear combination of solutions to Schrödinger's equation is also a solution. This suggests that one approximation to ψ would be a linear combination of two hydrogenic wave functions, ϕ_1 and ϕ_2, centered on protons 1 and 2 respectively:

$$(10)\quad |\psi\rangle = c_1|\phi_1\rangle + c_2|\phi_2\rangle$$

The real constants c_1 and c_2 are chosen to minimize the energy E′ given by

$$(11)\quad E' = \frac{\langle\psi|H_e|\psi\rangle}{\langle\psi|\psi\rangle} .$$

In terms of real hydrogenic states, this equation is

$$(12)\quad E'\left(c_1^2 + c_2^2 + 2c_1c_2\langle\phi_1|\phi_2\rangle\right) = c_1^2\langle\phi_1|H_e|\phi_1\rangle + c_2^2\langle\phi_2|H_e|\phi_2\rangle + 2c_1c_2\langle\phi_1|H_e|\phi_2\rangle$$

In order to minimize E′, the partial derivatives of E′ with respect to c_1 and c_2 must be zero. Applying these conditions to equation 12 results in two homogeneous equations:

$$(13a)\quad c_1\left(\langle\phi_1|H_e|\phi_1\rangle - E'\right) + c_2\left(\langle\phi_1|H_e|\phi_2\rangle - E'\langle\phi_1|\phi_2\rangle\right) = 0$$

$$(13b)\quad c_1\left(\langle\phi_1|H_e|\phi_2\rangle - E'\langle\phi_1|\phi_2\rangle\right) + c_2\left(\langle\phi_2|H_e|\phi_2\rangle - E'\right) = 0 .$$

These equations have a solution if the determinant of the coefficients of c_1 and c_2 is zero. Solving the determinant for E' and using the fact that $\langle\phi_1|H_e|\phi_1\rangle = \langle\phi_2|H_e|\phi_2\rangle$ for H_2^+ gives two energies,

$$(14a)\quad E'_+ = \frac{\langle\phi_1|H_e|\phi_1\rangle + \langle\phi_1|H_e|\phi_2\rangle}{1 + \langle\phi_1|\phi_2\rangle}$$

$$(14b)\quad E'_- = \frac{\langle\phi_1|H_e|\phi_1\rangle - \langle\phi_1|H_e|\phi_2\rangle}{1 - \langle\phi_1|\phi_2\rangle}$$

corresponding to the normalized eigenfunctions

$$(15a)\quad \psi_+ = \frac{\phi_1 + \phi_2}{\sqrt{2\left(1 + \langle\phi_1|\phi_2\rangle\right)}}$$

$$(15b)\quad \psi_- = \frac{\phi_1 - \phi_2}{\sqrt{2\left(1 - \langle\phi_1|\phi_2\rangle\right)}}.$$

E' and ψ can be evaluated once the wave functions ϕ_1 and ϕ_2 are chosen. In figures 1 and 2, two 1s orbitals of atomic hydrogen are used to calculate E' and ψ. As shown in figure 1, the energy E'_+ has a minimum at an internuclear distance R_{eq} which corresponds to a stable configuration of H_2^+. The energy E'_- lies above E'_+ for all intermediate internuclear distances, and has no minimum. Because of this behavior, ψ_+ is known as a bonding orbital and ψ_- is known as an antibonding orbital. These two types of molecular orbitals form the basis for the electronic states of diatomic molecules.

As illustrated in figure 2, the bonding orbital ψ_+ corresponds to an overlap of the two atomic orbitals $|\phi_1\rangle$ and $|\phi_2\rangle$. The electron density is higher between the two nuclei in the bonding orbital than in the

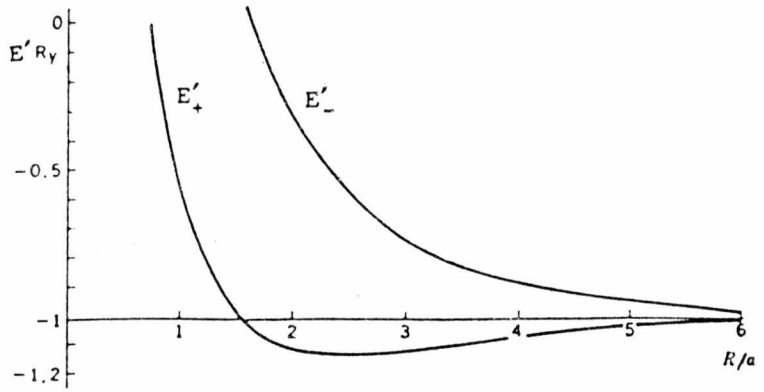

Figure 1. Energy levels for bonding and antibonding orbitals of H_2^+.

Source: David Park, Introduction to the Quantum Theory, Second Edition, (McGraw-Hill, New York, 1974), p. 501.

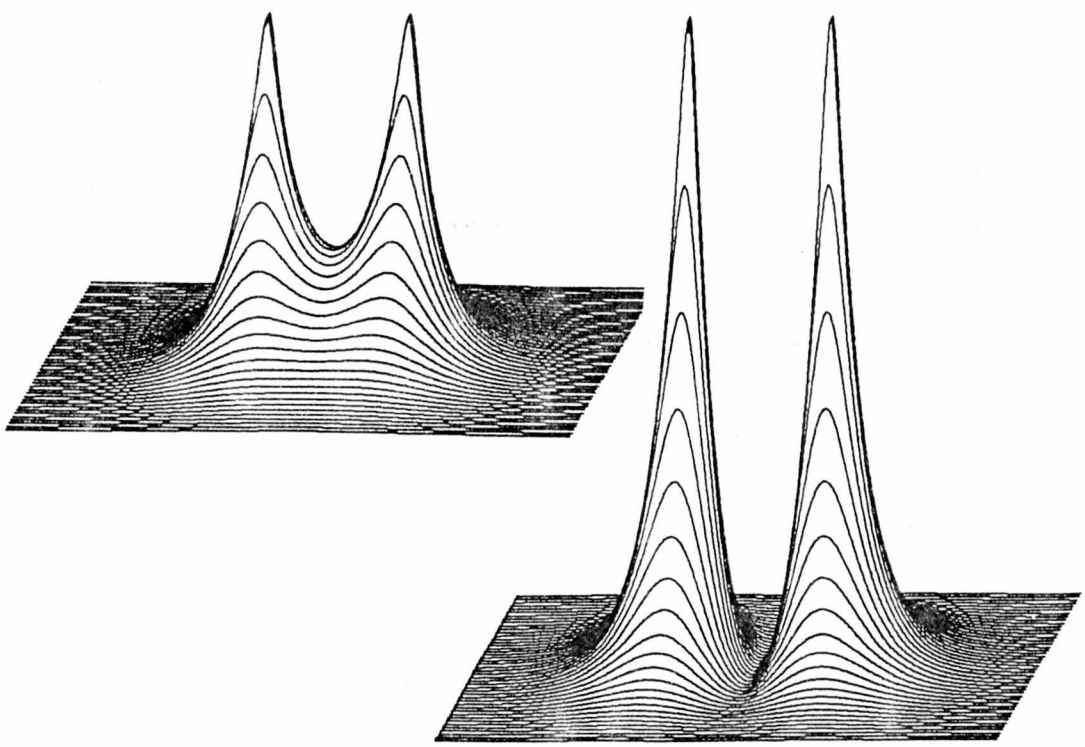

Figure 2. Electron densities for bonding (top) and antibonding (bottom) orbitals of H_2^+.

Source: David Park, Introduction to the Quantum Theory, Second Edition, (McGraw-Hill, New York, 1974), p. 505.

antibonding orbital. This build-up of charge effectively screens the nuclei from each other, lowering the energy of the system and creating a stable molecule. Atomic orbitals used to create bonding molecular orbitals in the LCAO approximation should be chosen so that they overlap to a considerable extent. A 1s and 2s combination, for example, would not produce as stable a state as two 1s or two 2s combinations.

The ground state of H_2^+ is formed from a combination of two 1s atomic orbitals with the electron in the ψ_+ molecular orbital. Excited states are formed by combining excited atomic states; 2s or 2p for example. When electronic states of more complex molecules containing more than one electron are considered within the LCAO approach, an additional approximation is made. The electron-electron correlation in the electronic Hamiltonian is ignored, in effect treating the electrons as independent particles. Only atomic orbitals from the valence shell of the constituent atoms are considered, since these loosely bound electrons participate more than inner shell electrons in the formation of the molecular bond. Molecular orbitals are calculated for each electron in the potential of the two nuclei by combining atomic orbitals. These molecular orbitals are then filled with electrons in agreement with the Pauli principle and Hund's rules. The electronic states of heteronuclear molecules are further complicated by the fact that $\langle\phi_1|H_e|\phi_1\rangle \neq \langle\phi_2|H_e|\phi_2\rangle$. Molecular orbitals of heteronuclear molecules also lack the parity symmetry of homonuclear molecules.

Because diatomic molecules possess axial symmetry about the line joining the two nuclei, eigenstates of the Hamiltonian are also

eigenstates of the component L_Z of the orbital angular momentum operator, with eigenvalues m_l. Since the potential created by the two nuclei is also invariant under reflection through any plane containing the nuclei, the energy of the stationary states depends only on the absolute value of m_l. The value of $|m_l|$ is used to label molecular orbitals in the LCAO approximation as follows:

$$
\begin{aligned}
&|m_l| = 0 \leftrightarrow \sigma \\
&|m_l| = 1 \leftrightarrow \pi \\
&|m_l| = 2 \leftrightarrow \delta \\
&\vdots
\end{aligned}
\tag{16}
$$

In homonuclear diatomic molecules, the potential is also invariant under reflection through the midpoint of the line joining the two nuclei. Molecular orbitals of homonuclear molecules can be additionally labeled according to the parity with respect to this midpoint; g (gerade) for even parity and u (ungerade) for odd. The electron in the ground state of H_2^+ is in the molecular orbital labeled $1\sigma_g$.

The complete molecular electronic state formed by all orbitals is labeled with a capital Greek letter corresponding to the total angular momentum projection eigenvalue $|M_L|$. The letters used for each $|M_L|$ value are the same as those used for the $|m_l|$ values of the molecular orbitals. Electrons have spin $\frac{1}{2}$, so the resultant spin S will be an integer or half integer depending on the total number of electrons in the molecule. The axial magnetic field induced by the orbital motion of the electrons with $|M_L| \neq 0$ causes S to precess about the internuclear axis with a constant component $\frac{h}{2\pi} M_S$ with possible values $M_S = S, S - 1, \ldots -S$. The multiplicity $2S + 1$ is added as a left superscript to the

term symbol. Thus the ground state of H_2^+ is denoted $1\sigma_g{}^2\Sigma$. The nomenclature used to specify molecular orbitals and terms is analogous to that used to label atomic orbitals and states in many-electron atoms.

The total molecular wave function is a product of the electronic wave functions derived above and solutions to equation 9 describing the nuclear motion. There are two types of nuclear motion possible for diatomic molecules: rotation of the nuclei about the center of mass of the molecule, and vibration of the nuclei about their equilibrium positions. Since the moment of inertia of the molecule depends on the internuclear separation, vibration of the nuclei affects the rotational motion. It will be shown that for small amplitude vibrations, the two types of motion can be separated.[9]

The radial wave equation for two nuclei of mass m_1 and m_2 is

$$(17)\quad \left[\frac{-h^2}{8\pi^2\mu}\frac{d^2}{dr^2} + \frac{l(l+1)h^2}{8\pi^2\mu r^2} + E'(r)\right]v_{v,l}(r) = E_{v,l}v_{v,l}(r),$$

where μ is the reduced mass of the system and v and l are quantum numbers used to label the vibrational and rotational states of the system. Because of the complex form of the effective potential E', only an approximate solution will be discussed that contains the important properties of the nuclear motion. The potential $E'(r)$ is first expanded in a Taylor series about the equilibrium position of the nuclei R_{eq} in order to obtain the vibrational energy levels:

$$(18)\quad E'(r) = -V_0 + a(r - R_{eq})^2 - b(r - R_{eq})^3 + \ldots$$

If terms of order three and higher in $(r - R_{eq})$ are neglected in the expansion, $E'(r)$ is a harmonic oscillator potential. Thus, for $l = 0$

and for small amplitude oscillations, the two nuclei can be modeled as a simple harmonic oscillator of mass μ . The vibrational energy levels are given by

$$(19)\quad E_{v,0} = -V_0 + \left(v + \frac{1}{2}\right) hf$$

$$v = 0,1,2...$$

where

$$(20)\quad f = \frac{1}{2\pi}\sqrt{\frac{2a}{\mu}}\,.$$

When n is large enough so that the third order term is not negligible in the Taylor expansion, the oscillator becomes anharmonic. In this case, the separation between energy levels is no longer constant, but increases as v increases.

For rotating molecules, the angular momentum quantum number l is no longer zero, and the centrifugal part of the potential in equation 17 contributes rotational energy to the system. The centrifugal part of the potential can be approximated by taking only the zeroth order term in its expansion about the equilibrium position R_{eq} of the nuclei:

$$(21)\quad \frac{l(l+1)h^2}{8\pi^2\mu r^2} \approx \frac{l(l+1)h^2}{8\pi^2\mu R_{eq}^2} = Bhl(l+1)\,.$$

Combining equation 21 with the first two terms in the expansion of E′ in equation 18 gives an approximation for the total effective potential in the radial wave equation. This is a good approximation, since $Bhl(l+1) \ll hf$ for small l values. With this additional approximation, equation 17 becomes

$$(22)\quad \left[\frac{-h^2}{8\pi^2\mu}\frac{d^2}{dr^2} + Bhl(l+1) - V_o + \left(v + \frac{1}{2}\right)hf\right]v_{v,l}(r) = E_{v,l}v_{v,l}(r),$$

where

$$(23)\quad B = \frac{h}{8\pi^2\mu R_{eq}^2}$$

The constant terms in the brackets can be subtracted from both sides of the equation. The equation then has the form of a harmonic oscillator equation with the terms on the right side equal to $(v + \frac{1}{2})hf$. The total energy of the nuclear motion in this approximation is then

$$(24)\quad E_{v,l} = -V_0 + (v + \tfrac{1}{2})hf + Bhl(l+1)$$

$$v = 0,1,2...$$

$$l = 0,1,2,..$$

In equation 24, the term $(v + \frac{1}{2})hf$ represents the vibrational energy of the molecule and $Bhl(l+1)$ represents the rotational energy. The rotational energy levels for adjacent l values are separated by 2Bhl.

A better approximation can be made if more terms in the expansion of the centrifugal part of the potential about the equilibrium position of the nuclei are included. It has already been noted that including higher order terms in the expansion of E′ causes anharmonic behavior of the vibrational part of the energy. Including more terms in the expansion of the centrifugal potential causes a shift in the location of the minimum of the effective potential in equation 17. The value and curvature of the effective potential at the new equilibrium position also change.

The energies associated with electronic, vibrational, and rotational transitions are on the order of 10 eV, 10^{-1} eV, and 10^{-3} eV

respectively. In general, all three types of transitions occur for energies above about 10 eV. Thus, electronic transitions contain structure from rotational and vibrational processes.[10]

The electronic and nuclear properties described above can now be used to explain molecular dissociation processes. The dissociation of diatomic molecules can be attributed to one of four general processes: formation of an unstable complex, electronic excitation to a repulsive state, predissociation, or vibrational or rotational excitation to the continuum.[5] Formation of an unstable intermediate projectile-target complex occurs at energies in the thermal range, and does not contribute much to collisional dissociation in the keV range.[3]

Figure 3 illustrates dissociation via electronic transitions to a repulsive state. The Frank-Condon principle governing electronic transitions states that these transitions occur so rapidly with respect to the vibrational motion of the nuclei that the nuclei have roughly the

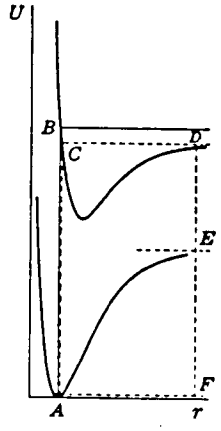

Figure 3. Dissociation via Frank-Condon transitions. Since the minima are displaced, transitions can only occur from A to B. B is above the dissociation limit.

Source: Gerhard Herzberg, Molecular Spectra and Molecular Structure, I. Spectra of Diatomic Molecules, Second Edition, (Van Nostrand Reinhold, New York, 1950), p. 195.

same relative positions and velocities after the transitions as they did before. The most probable transitions are those that occur without the nuclei undergoing large instantaneous changes in position or velocity.[10] Dissociation via electronic transitions produces dissociation fragments with well defined, often large, final kinetic energies in the center of mass frame of the dissociating molecule.

Predissociation is an example of a radiationless decomposition process. When one or more discrete energy levels of one term series overlap a continuous range of another term, mixing of the eigenfunctions can lead to dissociation. The system resonates between the discrete and continuous states. Once the system is in the continuous state, however, the molecule decomposes and cannot return to the discrete state. This process is analogous to the Auger process in atomic systems. Three different types of predissociation occur, corresponding to the three energy ranges found in molecular systems. The most important of these for diatomic molecules is overlapping of bound vibrational and rotational states of one electronic state with the dissociation continuum of another. Dissociation occurs after a radiationless transition to this dissociated electronic state. In polyatomic molecules, overlapping of a high vibrational state with the dissociation continuum joined to a lower dissociation limit of a single electronic state can cause an atom to split off of the molecule. This process is known as predissociation by vibration. The final type of predissociative decomposition is predissociation by rotation: overlapping of the higher rotational levels of a given vibrational level of a molecule with the dissociation continuum of the same electronic

state. In this process, the molecule decomposes without changing its electronic state.[10]

The final process, collisional dissociation of diatomic molecules by vibrational or rotational transitions to dissociative states, usually involves a large momentum transfer from the target to one or both of the projectile nuclei. If the internal energy of the molecule after the collision is higher than the dissociation energy of the initial vibrational state, the molecule will dissociate. Vibrational dissociation can be accompanied by a large displacement of the center of mass of the molecule from the initial direction of travel, but it is also possible for this process to occur without a large displacement of the center of mass; via an equal but opposite momentum transfer to both nuclei of the projectile for example.[10] The dissociation products produced by dissociation via vibrational or rotational transitions most often have near zero final kinetic energies in the center of mass frame of the dissociating molecule.

C. Two-body Threshold Laws

Threshold laws attempt to describe the energy dependence of the cross section for a process near the threshold energy for that process. Two-body threshold laws are useful in the description of processes that result in two widely separated particles with near zero relative kinetic energy. In this case, the laws describe the dependence of the cross section for these processes on this small kinetic energy. Two-body threshold laws were first investigated by Wigner in 1948.[11] Wigner

showed that the energy dependence of the cross section is a function of the long range potential between the reaction products only, regardless of the reaction mechanism that produced the two particles in the final state. In the present investigation, singly charged diatomic molecules dissociate after undergoing fast, large impact parameter collisions into two molecular fragments in their electronic ground states with near zero energy above the molecular dissociation limit. It will be argued below that the energy dependence of the dissociation cross section near threshold can be described by a two-body threshold law. Since the collisions are fast, i.e. the duration of the collision is much shorter than the inverse of a typical vibrational or rotational frequency of either atom in the projectile molecule, the target atom involved in the collision can be neglected when studying this energy dependence.

The cross section for dissociation in first order time dependant perturbation theory can be calculated in the center of mass frame of the dissociating molecule using Fermi's Golden Rule:

$$(25)\ \sigma = C|\langle f|H'|i\rangle|^2\rho(E)\,.$$

In this equation, C is a constant, the initial state $|i\rangle$ is a product of the wave function of the diatomic molecule in its electronic ground state, $|i_m\rangle$, and a plane wave representing the neutral target atom moving with velocity $\mathbf{v}_i$, $|i_a\rangle$. The final state $|f\rangle$ is a product of $|f_m\rangle$ representing the dissociation products moving in a long range potential with a small total energy E, and a plane wave, $|f_a\rangle$, representing the target atom moving with velocity $\mathbf{v}_f \approx \mathbf{v}_i$. H' is the perturbation induced by the collision, and $\rho(E)$ is the density of final states.

In terms of the wave number k, the density of final states is

$$(26)\ \rho \propto \frac{dn}{dE} \propto k^2 \frac{dk}{dE} \propto k \propto \sqrt{E}.$$

Thus the energy dependence of the cross section is given by the product of $\sqrt{E}$ and the energy dependence of $|\langle f|H'|i\rangle|^2$. The initial state $|i\rangle$ is independent of E. For collision energies much larger than the energy above threshold, E, the final atomic state $|f_a\rangle$ will change little for small changes in E. For small values of E then, the energy dependence of σ is contained in $|f_m\rangle$. The initial molecular state is well localized, so the major contribution to the overlap integral $\langle f_m|H'|i_m\rangle$ comes from a small region of space.

O'Malley[12] used a treatment based on the modified effective range theory[13] to study the energy dependence of the exact wave function $|f_m\rangle$ in a long range potential. He showed that if $|f_m\rangle$ is chosen to be energy independent in the small region of space in which the matrix element $\langle f_m|H'|i_m\rangle$ is evaluated, the major energy dependence of $|f_m\rangle$ comes from the energy dependence of a normalization factor required to match the asymptotic form of $|f_m\rangle$ to a plane wave at large distances. If the energy E is much smaller than the short range interaction energy of the two particles, the energy dependence of $\langle f_m|H'|i_m\rangle$ can be factored out into a normalization factor $\frac{1}{N(E)}$. The form of $\frac{1}{N(E)}$ is determined by the nature of the long range potential between the particles in the final state. The energy dependence of the cross section is then

$$(27)\ \sigma(E) \propto \sqrt{E} * \text{energy dependence of } N(E)^{-2}.$$

Wigner[11] calculated the energy dependence of the normalization factor for various interactions between the two particles in the final state: no interaction, attractive and repulsive Coulomb potentials, and the

angular momentum barrier potential. These are shown in Table 1 along with the energy dependence near threshold of the cross section $\sigma(E)$.

In the case of singly charged diatomic molecules dissociating into a neutral atom and a positively charged ion with zero relative angular momentum, l, the polarization potential $\frac{\alpha e^2}{2r^4}$ is the dominant long range potential. If the relative angular momentum of the two particles is not zero, the angular momentum barrier potential ($\alpha\ r^{-2}$) has a longer range than the polarization potential. The wave function of a particle moving in a r^{-4} potential with arbitrary angular momentum l has been calculated by O'Malley et al[13]. The cross section, with the normalization factor N(E) evaluated to second order in the wave number k, is given by

$$(28)\quad \sigma(E) = A\ k^{2l+1}\left[1 - \frac{4\ \beta^2\ k^2\ \ln k}{(2l+3)(2l+1)(2l-1)} + O(k^2)\right]$$

where $k = \sqrt{\frac{8\ \pi^2\ \mu\ E}{h^2}}$, $\beta = \sqrt{\frac{\alpha}{a}}$, $a = \frac{h^2}{4\ \pi^2\ \mu\ e}$, α is the

Table 1. Energy dependence of the normalization factor, N, and the cross section, σ, for various long range interactions.

Interaction	$N(E)^{-2}$	$\sigma(E)$
no interaction	constant	$\sqrt{E}$
attractive Coulomb $\left(\frac{-1}{r}\right)$	$E^{-1/2}$	constant
repulsive Coulomb $\left(\frac{1}{r}\right)$	$E^{-1/2}\exp\{CE^{-1/2}\}$	$\exp\{CE^{-1/2}\}$
angular momentum barrier $\left(\frac{l(l+1)}{r^2}\right)$	E^{l}	$E^{l+1/2}$

polarizability, A is a constant, and μ is the reduced mass of the particles. Hotop[14] et al have given the explicit form of equation 28 to third order in k for the case of zero relative angular momentum. The expansion in equation 28 is valid for $\beta k \ll 1$. The earlier assumption that the energy dependence of $\langle f_m|H'|i_m\rangle$ is contained in the normalization factor N(E) remains valid as long as $\sqrt{\frac{\beta}{k}}$ is less than a typical dimension of the initial bound state of the particle.

The energy dependence of the cross section is dominated by the long range angular momentum barrier potential ($\sigma(E) \alpha k^{2l+1}$) at very small values of k. Deviations from this simple energy dependence due to shorter range potentials already become important for energies E « 1 eV, and a simple expansion of N(E) in powers of k is no longer valid. This is true even in the energy range where N(E) contains the major energy dependence of the cross section, i.e. where threshold laws still apply.

As stated above, threshold laws apply when the total energy of the final products is small compared to the short range interaction energy. Since dissociation of molecules via electronic excitation produces final states with discrete fragment energies on the order of tens of eV, it is unlikely that threshold laws will describe the energy dependence of the cross section for this process. Vibrational and rotational processes on the other hand, create fragment ions with a continuous distribution of energies on the order of one eV and less. The energy of these ions is well below the dissociation energy of the parent molecules, so threshold laws cannot be ruled out on the basis of the final state energy.

D. The Experiments

The experiments conducted in this investigation are designed to test whether two-body threshold laws can be used to predict the energy dependence of the cross section for collisional dissociation of diatomic molecules. When fast ArH^+, N_2^+, and H_2^+ projectiles dissociate, the dissociation fragments with small total center of mass (CM) frame energies must travel in the lab frame with velocities close to the projectile velocity. Data from previous experiments indicated that a sufficient number of positive fragment ions travelling near the projectile velocity could be collected to make the present investigation feasible.[15] The lab frame energy E′ of a dissociation fragment from a homonuclear molecule emitted in the forward or backward direction in terms of the CM energy E can be obtained from the expression

$$(29)\quad E' = \frac{1}{2}\left(E'_o - E^*\right) \pm \left[E\left(E'_o - E^*\right)\right]^{1/2} + \frac{1}{2}E$$

where E'_o is the initial projectile energy and E^* is the amount of incident kinetic energy transformed to excitation energy of the ion or translational energy of the target.[16] As formula 29 indicates, small CM frame energies will be measured as large energies in the lab frame. The technique of looking at the dissociation fragments of a beam of molecular ions facilitates the measurements of the small CM frame energies of interest in this investigation.

In the present investigation, the projectile molecules are assumed to be in their electronic ground state since only one bound electronic state exists for ArH^+ and H_2^+, though they are probably in excited vibrational and rotational states. Of the four possible dissociation

channels discussed above, only dissociation by vibrational or rotational excitation is likely to create ionic dissociation fragments with small kinetic energy in their CM frame. Energy spectra in the lab frame of protons resulting from the dissociation of ArH^+ were measured previously (figure 4). The spectra show a central peak where the fragment ion velocity equals the beam velocity. This peak arises from collisional dissociation of the parent molecule by vibrational excitation. It is flanked by the characteristic side peaks that arise from dissociation due to electronic transitions. This mode of dissociation has been investigated by Durup[16], Fournier[17], and other investigators[1] in the energy spectra of dissociation products from H_2^+, D_2^+, and N_2^+. Vibrational excitation of the electronic ground state is dominated by large impact parameter collisions which will not result in a large deflection of the CM of the molecule after the collision. The present investigation focuses on fragments resulting from these large impact parameter collisions with near negligible deflections of the CM of the projectile molecule.

Positively charged dissociation fragments are only accepted by the energy analyzer used in this investigation if they are ejected in the forward or backward directions. These positive fragments are collected in coincidence with neutral dissociation fragments travelling in the beam direction. This insures both that there is little deflection of the center of mass of the molecule after the collision, and that the molecule dissociates into a neutral particle and a singly charged positive ion.

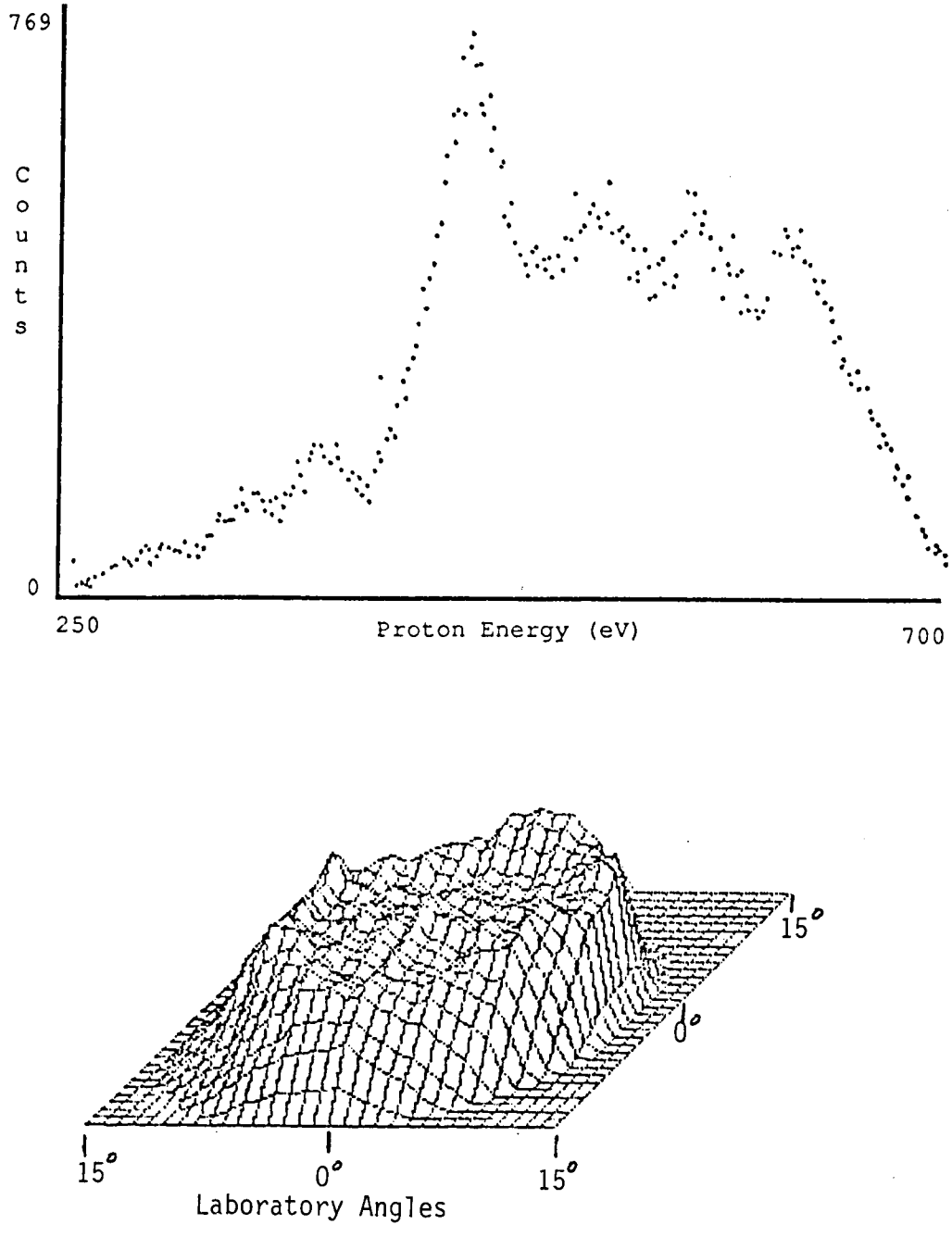

Figure 4. One (top) and two (bottom) dimensional spectra of protons resulting from the dissociation of 20 keV ArH^+ impacting on He. The one dimensional spectrum was taken using a channel electron multiplier by scanning the voltage applied to the proton analyzer over a 456 eV range centered on the beam energy. The two dimensional spectrum shows the angular distribution of the protons travelling with the beam velocity. It was taken using a circular channel plate detector with the proton analyzer set at the voltage corresponding to the peak in the energy spectrum.

Two-body threshold laws make two fundamental predictions about the energy dependence of the cross section which are tested in this investigation: i) $\sigma(E)$ is independent of the initial kinetic energy of the molecule, and ii) $\sigma(E)$ is independent of the reaction mechanism that creates the final fragments. In order to test the first prediction, ArH^+ ions are sent into collisions at two different energies. The second prediction is tested by using two different gas targets for all three molecular projectile ions. If two-body threshold laws apply to collisional dissociation, the energy dependence of the yields of H^+ from ArH^+ near threshold will be the same for the different beam energies and targets. Similarly, the yields of H^+ from H_2^+ and those of N^+ from N_2^+ near threshold will have the same energy dependence for both target gases used. The threshold laws do not predict that the ion yields will have the same energy dependence for each of the different molecular projectiles used if the interaction between the fragment ions is different in each case.

In summary, the goal of the experiments is to investigate the energy dependence of the cross section for collisional dissociation near threshold. Fragment ions with low center of mass frame energies resulting from large impact parameter collisional dissociation processes are studied. The initial energy of the projectile ions and the reaction mechanism that creates the fragment ions are varied. If the energy dependence of the fragment ion yields for the three projectiles used are each independent of the initial energies and target gases, it is likely that a two-body threshold law can be used to describe the cross section near threshold.

In order to accomplish these goals, new equipment was designed and built. In order to single out large impact parameter collisions resulting in a positively charged and a neutral fragment, both fragments must be detected in coincidence. Coincidence techniques also eliminate a large percentage of the background counts. The new equipment used to detect both fragments in coincidence is described in Chapter 2.

CHAPTER II

APPARATUS AND EXPERIMENTAL METHOD

A. Ion Source and Accelerator

The experimental apparatus used in this investigation, shown schematically in figure 5, consists of an ion source followed by an acceleration region, a 90° analyzing magnet, and a scattering chamber. The ion source can be raised to an adjustable extract potential, which floats on top of the potential applied to the accelerating region. A total energy of 60 keV is possible for singly charged ions. Beam currents on the order of μA are obtainable from the source. In the present investigation, the accelerator is used to create positive projectile ions. It is possible to create negative projectiles in the source, and to accelerate them by changing the polarity of the extract and acceleration power supplies. Four NRC hot oil diffusion pumps maintain the vacuum in the entire beam line at approximately 2×10^{-6} torr.

The singly charged positive diatomic molecular ions used as projectiles in these experiments are created in a Colutron model 101-Q ion source. Gas introduced into the source region at pressures between 50 and 250 mTorr is ionized by the arc discharge from a heated filament to an anode. The filament is maintained at a potential of -90 volts with respect to the anode. The arc current is kept below 0.5 A by adjusting the amount of current heating the filament. A mixture of

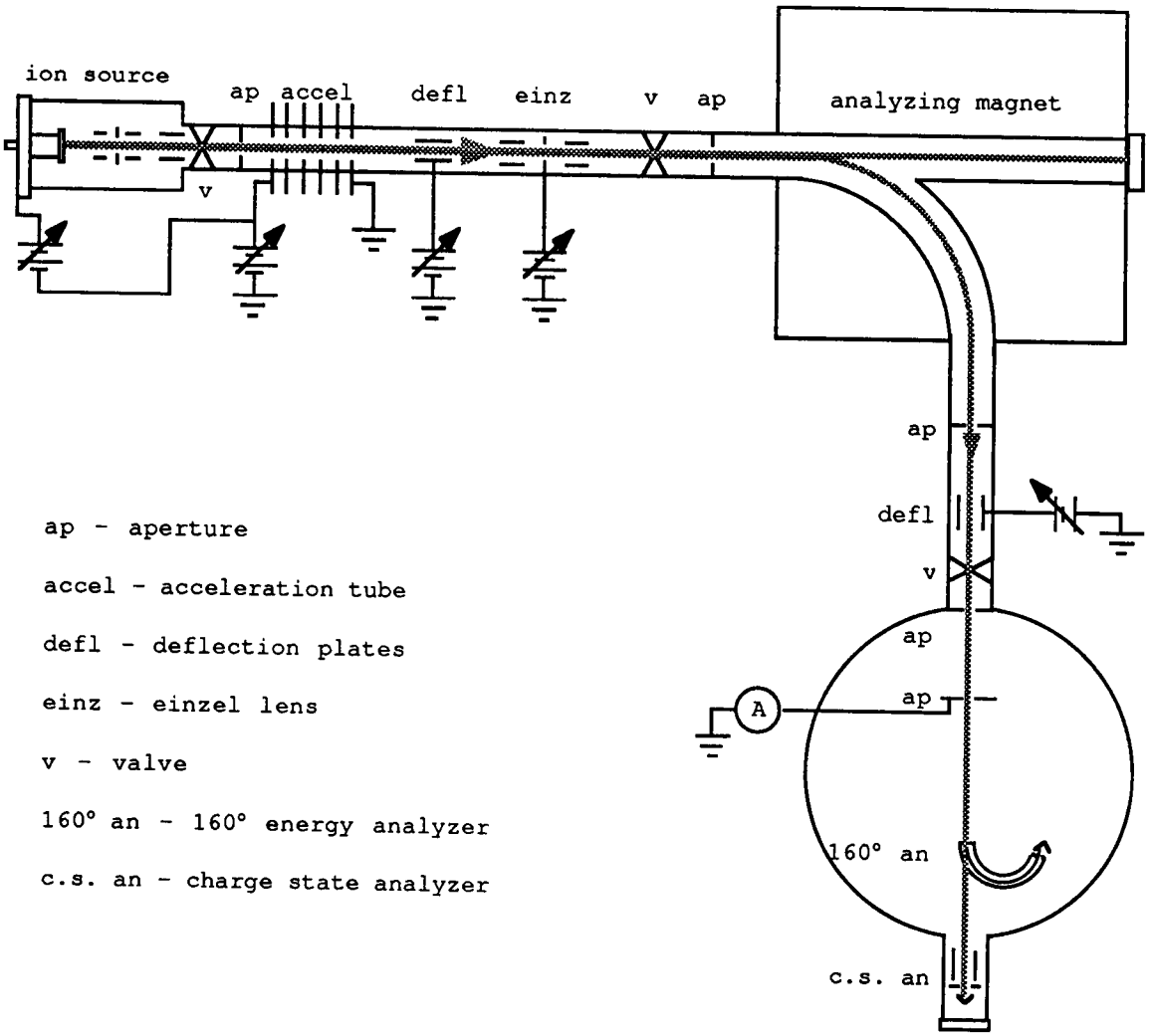

ap - aperture

accel - acceleration tube

defl - deflection plates

einz - einzel lens

v - valve

160° an - 160° energy analyzer

c.s. an - charge state analyzer

Figure 5. The accelerator.

argon and hydrogen is used to create the ArH^+ projectiles, and methane gas is used to create H_2^+. Durup et al[16] and Brenton et al[18] found that the shape of the peaks in the energy spectrum of protons resulting from the dissociation of H_2^+ depends on the source conditions used to produce the projectiles. Therefore, source conditions for different experiments with the same projectile are duplicated as closely as possible for each experiment. Figure 6 shows an exploded view of the complete ion source.

Projectile molecular ions are extracted from the source region at one to four keV and enter the acceleration tube where they are accelerated to the collision energy. The ions are then steered and focused onto a square aperture 2mm on a side located at one focal point of a 90° analyzing magnet capable of a momentum resolution of 1 part in 10^5. The projectile of interest is momentum analyzed and exits the magnet through a 1mm diameter circular aperture located at the exit focus of the magnet. A circular aperture 0.4mm in diameter placed 1.2m downstream from this aperture limits the angular spread in the beam to

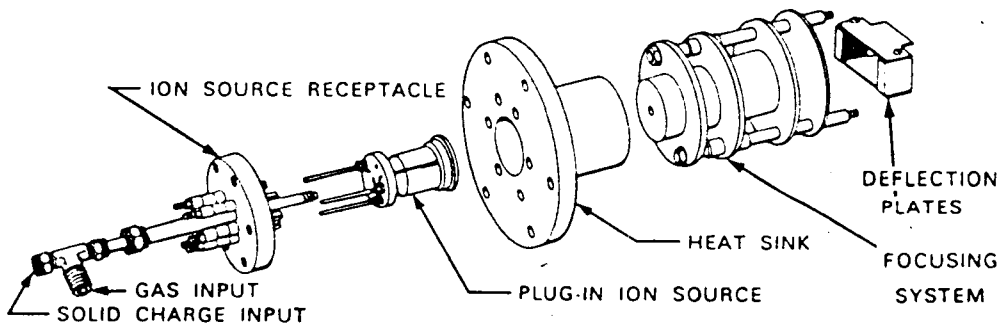

Figure 6. An exploded view of the ion source.
Courtesy of Colutron Research Corporation

5×10^{-4}rad as the beam enters the collision chamber. The beam spread is further restricted by another 0.4mm diameter circular skimming aperture inside the chamber, which is used to monitor the beam current before the beam enters the analyzer.

After passing through the skimming aperture, the projectiles enter a 13.5mm long cylindrical gas cell bounded by two 1.3mm diameter circular apertures. The center of the gas cell is located at one focal point of an electrostatic energy analyzer. Here some of the projectile ions collide with a neutral gas target and dissociate. In order to reduce the number of dissociations caused by collisions with background gas molecules, the vacuum in the chamber is maintained at 3×10^{-6} torr or less by an eight inch NRC hot oil diffusion pump located under the chamber, even when the gas is introduced into the gas cell. Neutral dissociation fragments and molecular projectile ions not involved in collisions exit the chamber and enter the charge state analyzer. The positive fragments are energy analyzed.

B. The Electrostatic Analyzer

In the present work, a 160° spherical sector analyzer is used to energy analyze the positive molecular fragments resulting from the dissociation. The idea of using a spherical condenser as an energy analyzer for charged particles was first introduced by Aston in 1919.[19] Since then, many authors have used these analyzers and described their properties in detail.[20] A schematic of a spherical sector electrostatic analyzer is shown in figure 7.

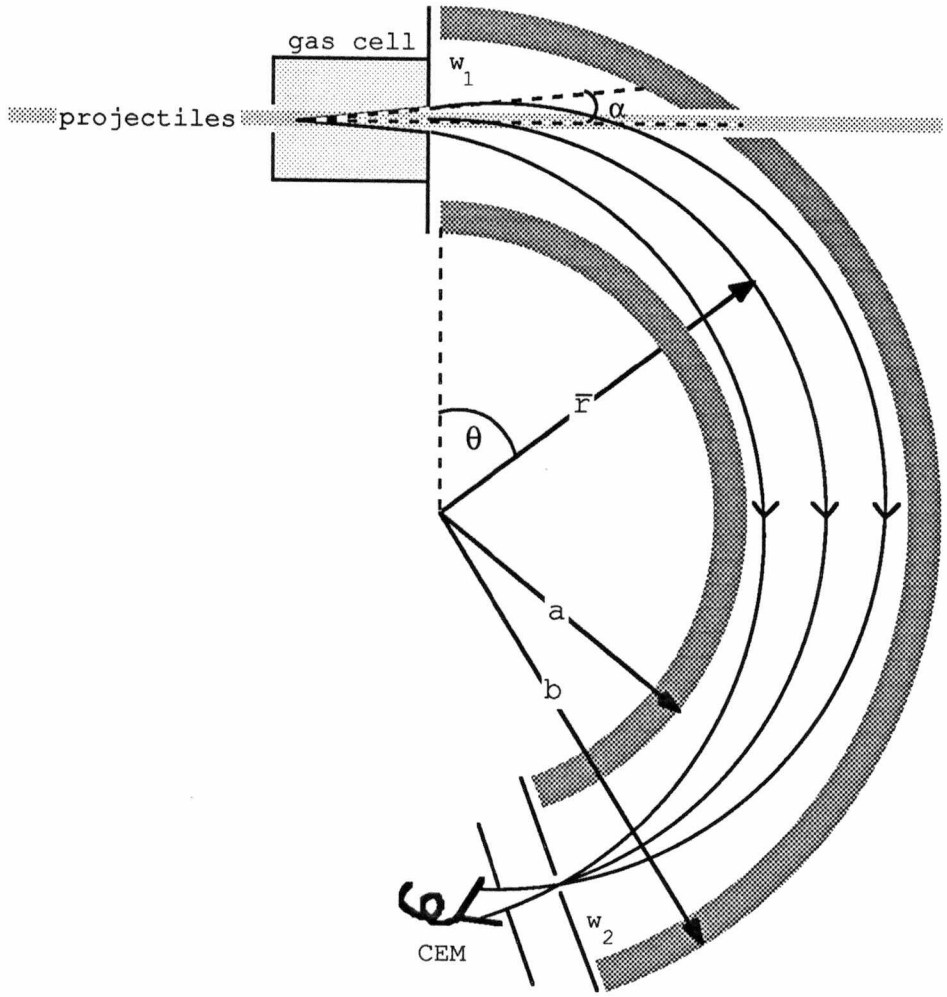

Figure 7. A 160° spherical sector analyzer.

The analyzer consists of two concentric copper spherical sectors of radii a and b separated by a small gap. A positive voltage is applied to the outer sector, and a negative voltage to the inner one. The total voltage V is divided in such a way that the central ray of the analyzer is at zero potential. The resulting field in the analyzer is radial and is given by $\left(\frac{V}{r^2}\right) \frac{ab}{b - a}$. For electrostatic analyzers, the analyzer constant C gives the relationship between the energy E′ of a particle

with charge q travelling along the central ray, and the applied voltage V; $C = \frac{qV}{E'}$. A spherical sector analyzer has an analyzer constant given by

$$(30)\quad C = \frac{b}{a} - \frac{a}{b} .$$

For the spectrometer used in this investigation, C = 0.44.

The differential equation of motion for a charged particle entering the analyzer at an arbitrary r_o is

$$(31)\quad \frac{d^2U}{d\theta^2} + U = \frac{\bar{r}E'_o}{r_o E' \cos^2\alpha} ,$$

where $U = \frac{r_o}{r}$, $\bar{r} = \frac{1}{2}(a + b)$, and the angle α in the plane of the analyzer is measured from the direction of the central ray. The solution of equation 31 is

$$(32)\quad \frac{r_o}{r} = \frac{\bar{r}\, E'_o\, (1 - \cos\theta)}{r_o E' \cos^2\alpha} + \cos\theta - \tan\alpha \sin\theta.$$

A power series expansion of equation 32 in α contains all powers of α. For $\theta = 180°$, however, the last term in equation 32 is zero. Since this term contains the only first power in α, the expansion will contain no first order terms in α for $\theta = 180°$. Thus the analyzer provides first order focusing in the plane of the analyzer for $\theta = 180°$. Because of the spherical symmetry, the spectrometer provides perfect focusing in the direction perpendicular to the plane of the analyzer.

The dispersion D of an analyzer is defined as the displacement of the image position per fractional change in energy. It is desirable to have as large a dispersion as possible. The dispersion of the spherical sector analyzer is $2\bar{r}$. The transmission function of the analyzer

expresses the probability for transmission of a charged particle entering the analyzer with energy E′. It can be approximated by a trapezoid characterized by its top width, base width, FWHM, and area. These quantities are given in table 2 for an aberration free spectrometer, where w_1 and w_2 are the sizes of the entrance and exit apertures shown in figure 7. In the present investigation, w_1 = 1.3mm, w_2 = 1.45mm, and D = 109mm. The energy resolution of the spectrometer including aberrations is

$$(33)\quad \frac{\Delta E'}{E'} = \frac{w_2}{D} + O(\alpha^2).$$

For the spectrometer used in the present investigation, the energy resolution is approximately 1.4%.

A 180° spherical sector analyzer has the disadvantage of placing the object and image points at the boundaries of the sector field

Table 2. Constants for the transmission function, f, of an aberration free spectrometer.

Quantity	$w_1 > w_2$	$w_1 < w_2$	$w_1 = w_2 = w$
base width: $\frac{\Delta E'}{E'}$	$\frac{w_1 + w_2}{D}$	$\frac{w_1 + w_2}{D}$	$\frac{2w}{D}$
top width: $\frac{\Delta E'}{E'}$	$\frac{w_1 - w_2}{D}$	$\frac{w_2 - w_1}{D}$	0
$\frac{FWHM}{E'}$	$\frac{w_1}{D}$	$\frac{w_2}{D}$	$\frac{w}{D}$
area: $\int f\, dE'$	$\frac{E'w_2}{D}$	$\frac{E'w_2}{D}$	$\frac{E'w}{D}$

Source: K.D. Sevier, Low Energy Electron Spectrometry, (Wiley-Interscience, New York, 1972), p. 23.

region. Placing a target at the object point would distort the radial electric field at the sector boundary. Using a sector angle of 160° removes the object and image points from the sector boundaries while still preserving the focusing properties of a 180° analyzer to a good degree. For this reason, a 160° sector analyzer was used in the present work. The gas cell was placed at the object point, and a CEM was mounted 34.7mm from the image point behind a circular 2.5mm diameter aperture. The 2.5mm aperture along with w_2 limited the angular acceptance half-angle of the CEM to 0.036 rad. In some measurements, the CEM was moved farther from the image point, thus decreasing the acceptance half-angle to 0.025 rad.

C. The Charge State Analyzer

Previous experiments conducted with the accelerator used a Faraday cup at the exit port of the chamber to collect the beam. The current from the cup was monitored by a digitizer that output a pulse after a predetermined amount of charge had been collected. These pulses were fed into a scaler and used to step the voltage on the energy analyzer. Using the direct beam current for normalization integrates over all beam particles and does not allow individual particles to be counted. For the coincidence measurements in the present investigation, a method of deflecting charged particles out of the beam path and counting the remaining neutral fragments individually is needed.

A set of deflection plates is used to deflect the charged particles out of the beam path. A channel electron multiplier (CEM)

operating in pulse mode is mounted behind the chamber exit downstream from the plates, and used to collect the neutral particles. Electron avalanches caused by a particle striking the CEM create a fast potential change at its electrodes. This potential drop signals the arrival of a particle at the back of the Faraday cup. Individual particles can be counted as long as the count rate is low enough to avoid saturation of the CEM. In order to allow counting of neutrals or ions of a selected charge state, the CEM and deflection plates are integrated into a charge state analyzer.

The charge state analyzer used in these experiments, shown schematically in figure 8, consists of a set of 15cm long deflection plates separated by 2cm and located 15cm in front of a moveable CEM. A voltage of V volts applied across the plates will cause a deflection of $84.4 \frac{QV}{E'}$cm for a particle of energy E' (eV), and charge Q. A Faraday cup located downstream from the deflection plates collects the beam. A CEM is mounted at the rear of the cup on a stage capable of horizontal and vertical movement. The movement in either direction is measured by two linear motion feedthroughs mounted 90° apart on a cross housing the Faraday cup. Total horizontal and vertical displacements of 25mm and 8mm respectively are possible. By applying an appropriate voltage across the deflection plates, singly charged negative and positive particles are deflected into two distinct positions on the back of the cup, while the neutral particles remain undeflected. The CEM can be moved horizontally to collect ions or neutrals in one of the three positions.

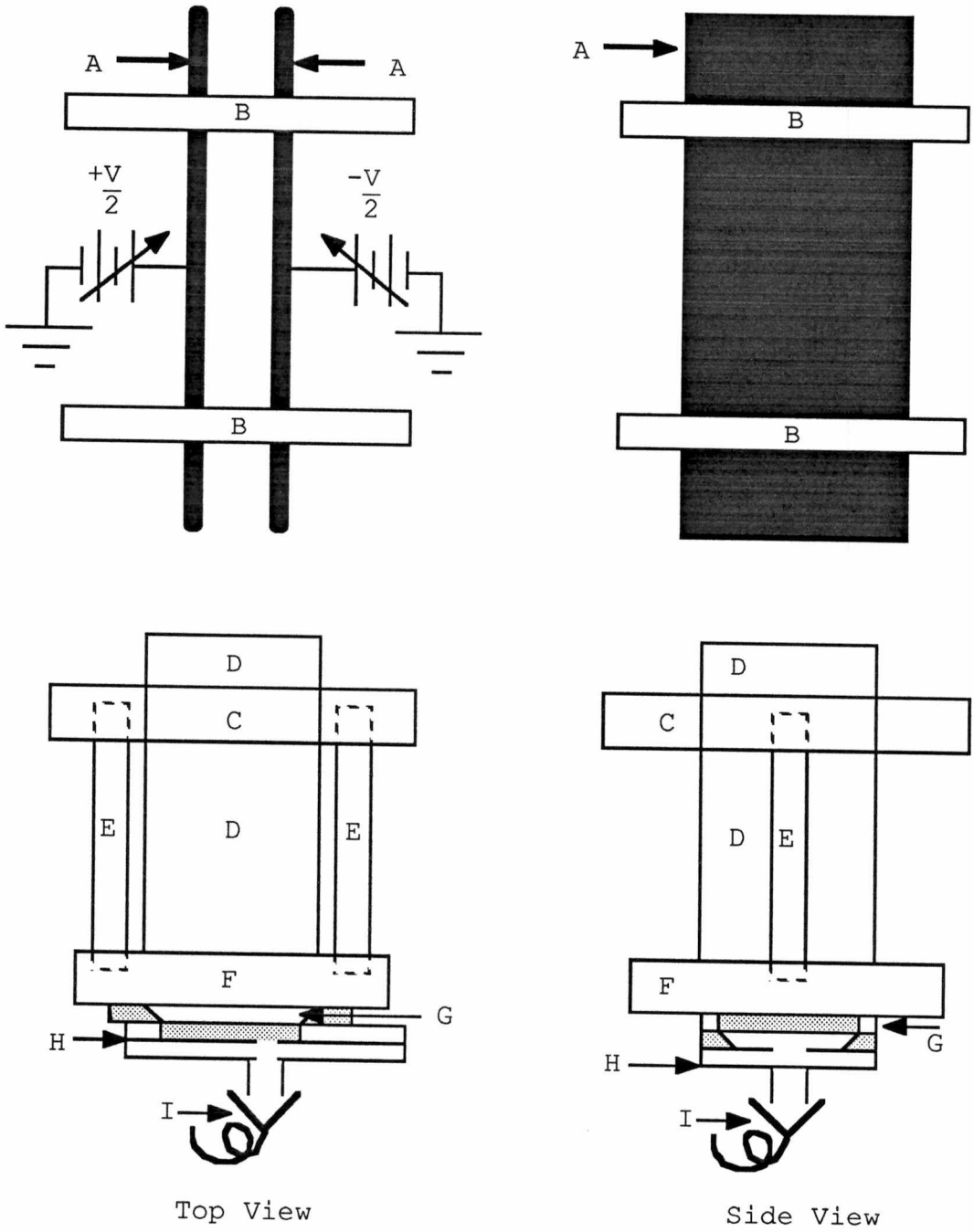

A - deflection plates
B - deflection plate supports
C - Faraday cup support
D - Faraday cup
E - support rods
F - support for moveable stage
G - vertical stage
H - horizontal stage with aperture and CEM
I - Faraday cup CEM

Figure 8. The charge state analyzer.

The CEM is mounted 10.7mm behind a 4mm diameter circular aperture at the back of the cup in order to reduce the likelihood of detecting scattered particles. A definite peak in the count rate from the CEM can be seen while moving the stage containing the aperture in and out of the beam path. When this stage is moved to its extreme position on either side, the rear of the cup remains sealed and the beam current entering the Faraday can be measured.

In the present work, the charge state analyzer is only used to detect neutral particles travelling in the direction of the main beam. The deflection plates are used to sweep all charged particles out of the beam path before they reach the CEM. Before taking data, the beam in the Faraday cup is maximized with the CEM moved to one side and no voltage applied to the deflection plates. This step insures that the undeflected beam travels unscattered into the cup after exiting the electrostatic analyzer. A voltage high enough to sweep all charged particles out of the original beam path is then applied to the plates, and the CEM is moved into the path of the neutrals.

D. Electronics and Data Acquisition

A typical data acquisition session proceeds as follows. The beam current is first maximized in the Faraday cup as described in section C. This insures that the beam is steered properly through the apertures and the spectrometer. The charge state analyzer CEM is then moved into the path of the neutral fragments and all charged particles are swept out of the beam path with the deflection plates.

The data are acquired using a LeCroy 3500 multichannel analyzer (MCA). Three LeCroy 3521 multichannel scaling modules (MCS) operating in histogramming mode and one LeCroy 3511 analog to digital converter (ADC) are used to take the data. MCS1 is used to collect raw data, and MCS2 and MCS3 collect the coincidence data as described below. The energy spectra are taken by stepping the voltage V applied across the spherical sectors of the energy analyzer after a predetermined number of neutral projectiles have been counted by the channel electron multiplier at the rear end of the Faraday cup (CEM_F). For each voltage applied to the spectrometer, only those ions with energy near V/C are transmitted by the spectrometer and counted, where C is the analyzer constant given in equation 30.

The MCA stores the counts accumulated during the time each voltage is applied to the spectrometer in a specific channel. After each voltage step, the channel number is incremented by one. Each channel corresponds to a certain voltage applied to the spectrometer. The channel number is output in binary form by MCS1 and input into a digital to analog converter (DAC). The DAC converts the binary channel number to an analog signal used to program the spectrometer power supply. When the channel number is incremented, the power supply output increases. The MCS modules and the ADC are gated off during voltage steps and do not count input signals when the analyzer voltage is not well-defined.

MCS1 receives the total number of charged fragment ions that are energy analyzed. MCS2 and MCS3 receive the number of charged fragments collected in coincidence with a neutral fragment. These coincidence data are taken using the signals from both the spectrometer channel

electron multiplier (CEM_S) and CEM_F. Output pulses from both CEMs are amplified and shaped by ORTEC 579 fast timing amplifiers and input into ORTEC 473A constant fraction discriminators. Fast negative NIM signals from the discriminators are input as start and stop signals into two ORTEC 567 time to pulse height converters (TPHC). The signals from CEM_S are used as start signals for the TPHC. If a stop signal from CEM_F arrives within a preset time interval, the TPHC outputs a positive pulse with an amplitude between 0 and 10 volts proportional to the elapsed time between the start and stop signals. The pulse height of this positive pulse is digitized by the ADC. This digitized signal is passed to the MCA as a channel number, and the MCA increments the number of counts in that channel by one.

The TPHC also contains a single channel scaler (SCA) which outputs a positive TTL logic pulse for each valid conversion whose output falls within a preset window. The SCA windows are set by observing the ADC spectrum. Figure 9 shows a typical ADC spectrum with the scaler window settings. The peak in the spectrum is produced by positive fragment ions that are created together with neutral fragments during dissociation. Thus, the peak corresponds to real coincidence events between the positive and neutral fragments. The background in the spectrum is caused by random coincidence events between a neutral fragment and an ion. One TPHC SCA window includes the coincidence peak in the ADC spectrum, and the other includes an equal number of channels covering the background. The SCA output pulses corresponding to counts in the coincidence peak are input into MCS2 and pulses

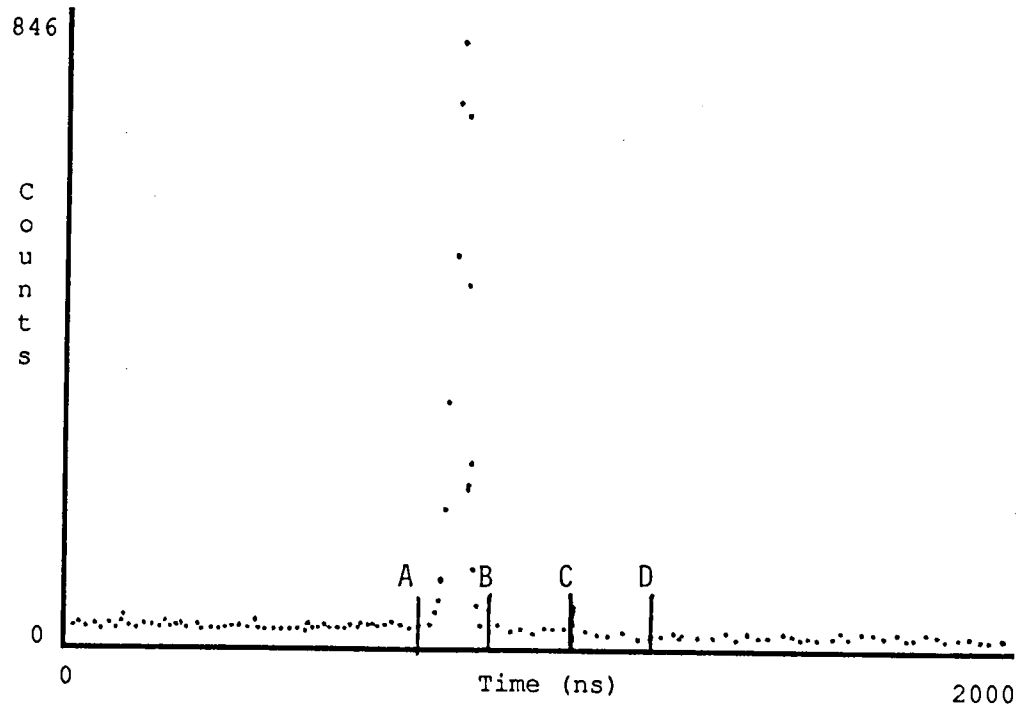

Figure 9. A typical ADC spectrum showing the peak (A -> B) and background (C -> D) scaler window settings. The peak corresponds to fragment ions detected in coincidence with neutral particles.

corresponding to background counts are input into MCS3. A schematic of the electronics used to take data is shown in figure 10.

After an energy spectrum has been measured, all data stored in the memory of the MCA by the three MCS modules and the ADC are written to magnetic floppy disks. The spectra from MCS1 and the ADC are not further analyzed. The analysis of the coincidence data from MCS2 and MCS3 is described in Chapter 3.

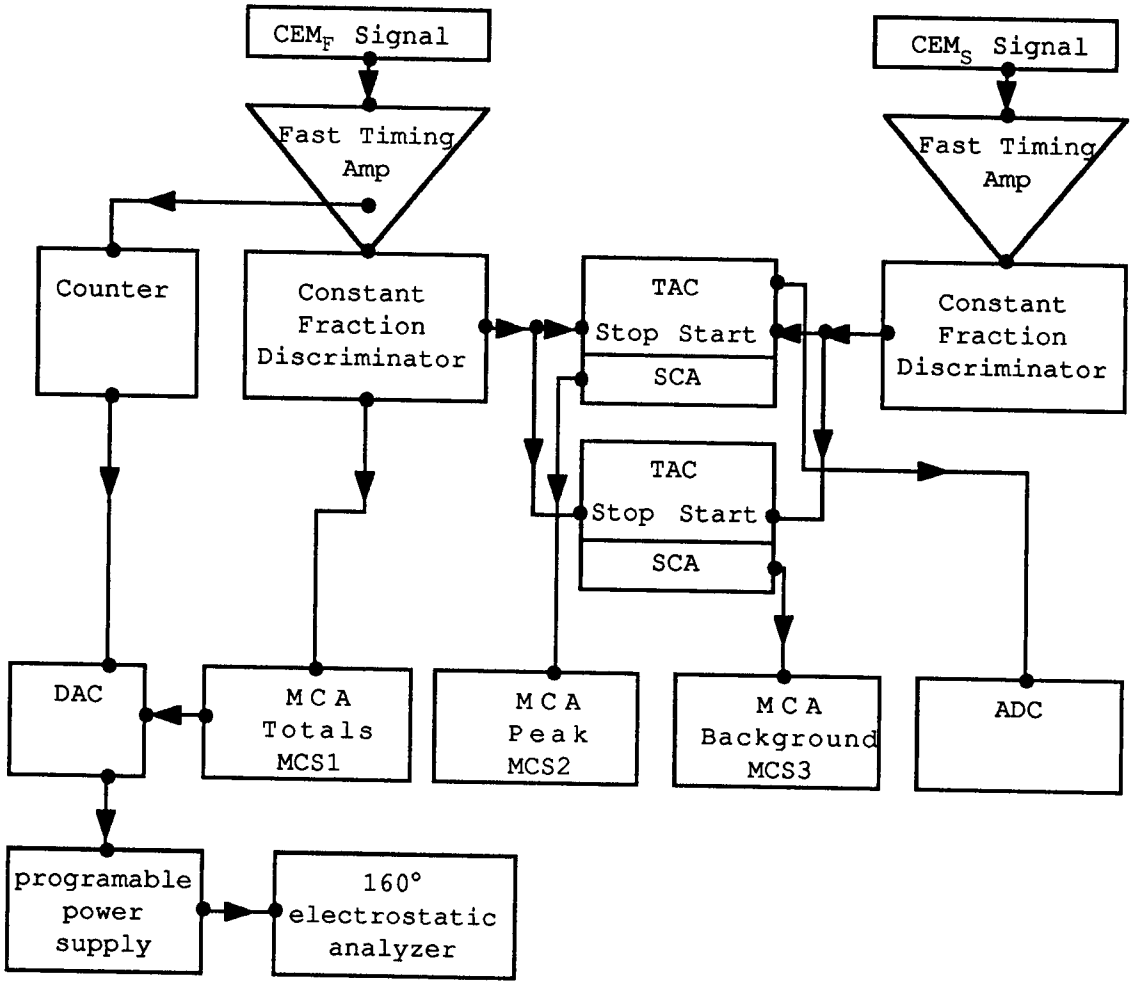

Figure 10. A schematic of the data acquisition electronics.

CHAPTER III

DATA ANALYSIS AND RESULTS

A. Treatment of the Raw Data

The purpose of this investigation is to determine whether the energy dependence of the cross section for collisional dissociation of diatomic molecules near threshold agrees with the predictions of a two-body threshold law. To this end, it is necessary to extract the energy dependence of the dissociation cross section from the energy spectra of the molecular dissociation fragments measured in the laboratory frame.

Each data point in an energy spectrum represents the number of positive fragment ions transmitted through the energy analyzer when a certain voltage is applied across the plates. This number can be expressed in the laboratory frame as

$$(34)\quad N = \int_{\Delta v'} \int_{\Delta \Omega'} P(\mathbf{v}') T(v',\Omega') v'^2 dv' d\Omega'$$

where $T(v',\Omega')$ is the transmission function of the analyzer discussed in Chapter 2, $P(\mathbf{v}')$ is the probability that a positively charged ion is ejected with velocity $\mathbf{v}'$ after the molecule dissociates, and $v'^2 dv' d\Omega'$ is a volume in velocity space. The number N in equation 34 is unique and must be the same in any coordinate frame. In particular, it must be the same in the laboratory frame and in the center of mass (CM) frame of the dissociation fragments. The number of ions detected in a given channel of the energy spectrum can then be expressed in the CM frame as

$$(35)\quad N = \int_{\Delta v}\int_{\Delta\Omega} P(\mathbf{v})\,T(v,\Omega)\,v^2 dv d\Omega$$

where $T(v,\Omega)$ and $P(\mathbf{v})$ denote the same quantities as in equation 34, but now in terms of the fragment ion velocity in the CM frame, v, and the solid angle in the CM frame, Ω. The volume in velocity space is the same in equations 34 and 35, and $P(\mathbf{v})$ is the same as $P(\mathbf{v}')$. For an isotropic distribution of fragments, $P(\mathbf{v}) = v^{-2}P(v)$. The quantity of interest here is $P(v)$, since $P(v)dv = P(E)dE$ and $P(E)$ is proportional to $\sigma(E)$. For reasons discussed below, an isotropic distribution of fragment ions in the projectile CM frame is assumed. Finding the dependence of $P(v)$ on v from the data, then, is equivalent to finding the energy dependence of the dissociation cross section $\sigma(E)$.

A single data point does not directly yield $P(v)$. Because of the finite energy and angular resolution of the 160° energy analyzer, ions with energies in a small interval around the nominal energy value corresponding to the voltage on the plates are transmitted. Therefore, each data point is actually an integral of $P(v)$ over a finite volume in velocity space, $(\delta v)^3$. When the velocity v is large, the dimensions of the volume over which $P(v)$ is integrated are small compared to v. Since $P(v)$ is expected to be a smoothly varying function of v in this region, it can be approximated by a constant over the integration volume. $P(v)$ can then be factored out of the integral and solved for by dividing N by the integral of $dvd\Omega$ over the velocity and solid angle intervals. Thus, data points in the velocity range $v \gg 0$ yield $P(v)$ directly. When v is small, however, the dimensions of the integration volume $(\delta v)^3$ are large compared to v, and $P(v)$ is rapidly changing within this volume.

In this velocity range, P(v) cannot be approximated by a constant, and factoring P(v) out of the integral as before does not yield meaningful results. Therefore, the region around the peak in the energy spectrum must be deconvoluted in order to obtain P(v). Lower energy resolution of the analyzer and a larger acceptance angle for the CEM increase the value of v at which a deconvolution process must be used to extract P(v) from the data.

With this in mind, a tradeoff was made when choosing the apertures defining the energy resolution of the analyzer and the acceptance angle of the CEM. In the measurements made here, energies of the dissociation fragments are in a range for which the detection efficiency of channel electron multipliers (CEM's) is low: roughly 250eV/amu (figure 11). The positively charged particles can be accelerated into the CEM to bring their energy into a range of greater counting efficiency, but the neutral fragments must be be detected at low energies. In order to achieve reasonable count rates in the Faraday cup CEM, the beam spot size cannot be made arbitrarily small. Since the entrance aperture of the analyzer must be larger than the beam size, the beam spot size

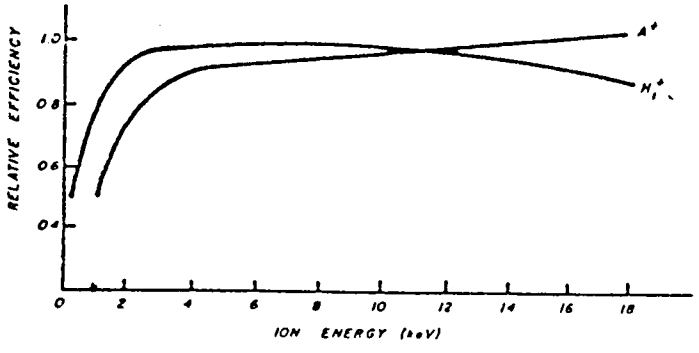

Figure 11. Relative detection efficiency of channel electron multipliers vs ion energy for protons and Ar^+ ions.

Source: Am. Laboratory , 67 (1979).

determines the size of this aperture. In order to insure that as many fragment ions as possible are transmitted through the analyzer and strike the CEM, the exit aperture is made slightly larger than the entrance aperture. Finally, the angle defining aperture must be larger than the exit aperture to give a well defined acceptance angle. Thus the need to keep the count rate high enough to obtain good counting statistics necessitates choosing large values for the energy resolution and acceptance angle, and makes deconvolution necessary.

B. Data Analysis

The first step in the analysis of the data is to subtract the random coincidence spectra from the true coincidence data. Each data point in the spectrum from MCS3 is subtracted from the corresponding data point in MCS2. Any negative values are set to zero. The result of this subtraction for a typical coincidence spectrum is shown in figure 12. Since low energy resolution and a large acceptance angle are used when taking data, the spectra must be deconvoluted to obtain P(v).

Each spectrum consists of data points taken at regular intervals $\Delta E'$ in the laboratory frame, where $\Delta E'$ is smaller than the energy resolution of the energy analyzer. Each data point is associated with a lab energy $E' = \frac{V}{C}$ and a lab velocity $v' = \sqrt{\frac{2E'}{m}}$ where V is the voltage across the analyzer plates, C is the analyzer constant defined in equation 30, and m is the mass of the singly charged molecular fragment. Data points near the peak, in the interval $v'' = 0 \rightarrow v_h$ for the forward direction and $v'' = 0 \rightarrow v_l$ for the backward direction, are fit with a

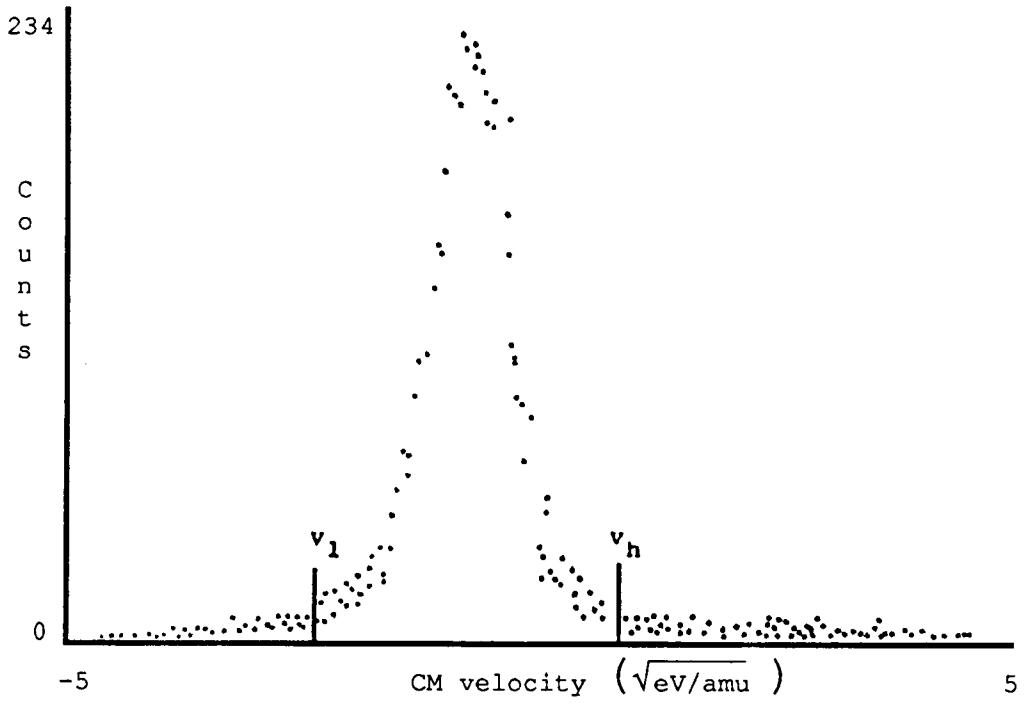

Figure 12. A coincidence spectrum measured for 10 keV ArH^+ impacting on Xe. The data go to zero above v_h and below v_l.

high degree polynomial in v". The parameter v" is defined as $v' - v_p$, where v_p is the initial velocity of the projectile. Data points above v_h and below v_l are fit to a polynomial in v''^{-1}. This procedure interpolates between the steps in energy. This is done in order to obtain an effective measured data point for any v". The measured data points go to zero above and below some velocity on each side of the peak, v_h and v_l in figure 12. P(v) is assumed to drop to zero rapidly above v_h and below v_l, so data points in these regions are fit to a polynomial in $\frac{1}{v''}$. The polynomial fits in v" are matched to the fits in $\frac{1}{v''}$ at v_h and v_l for the forward and backward directions respectively in order to produce smooth curves.

As stated earlier, the distribution of fragment ions is assumed to be isotropic. Limited measurements of the complete velocity distribution of protons resulting from the dissociation of ArH^+ at one collision energy made earlier at low resolution show no anisotropy in the distribution of protons emitted with near zero velocity in the CM frame. Data taken in the current investigation show no forward-backward anisotropy after corrections for instrumental effects are made. The assumption of isotropy is further tested in the current investigation by making measurements with N_2^+ and ArH^+ projectiles using two different acceptance angles. The data are consistent with an isotropic distribution of fragment ions in the CM frame of the projectile molecule.

In order to deconvolute the data, the spectra are split into two parts: that part corresponding to ions ejected in the forward direction, and that part corresponding to ions ejected in the backward direction. For the forward direction, the velocity interval from v" = 0 to v" = v_h is divided into a large, fixed number of concentric circular shells with the center at the beam velocity, as shown in figure 13. Each shell with outer radius v_j, inner radius v_{j+1}, and volume U_j is labeled with the index j and associated with the probability $P(v_j)$. When a voltage is applied to the analyzer plates, all positive ions ejected into the volume $(\delta v)^3$ are transmitted by the analyzer and counted. This volume is bounded by the planes labeled v_- and v_+ in figure 13 and the acceptance cone of the CEM. The planes v_- and v_+ are separated by $\delta v = v\left(\frac{\Delta E'}{2E}\right)$. During the deconvolution process, the value of v_- is stepped such that it always lies on a shell boundary. In figure 13,

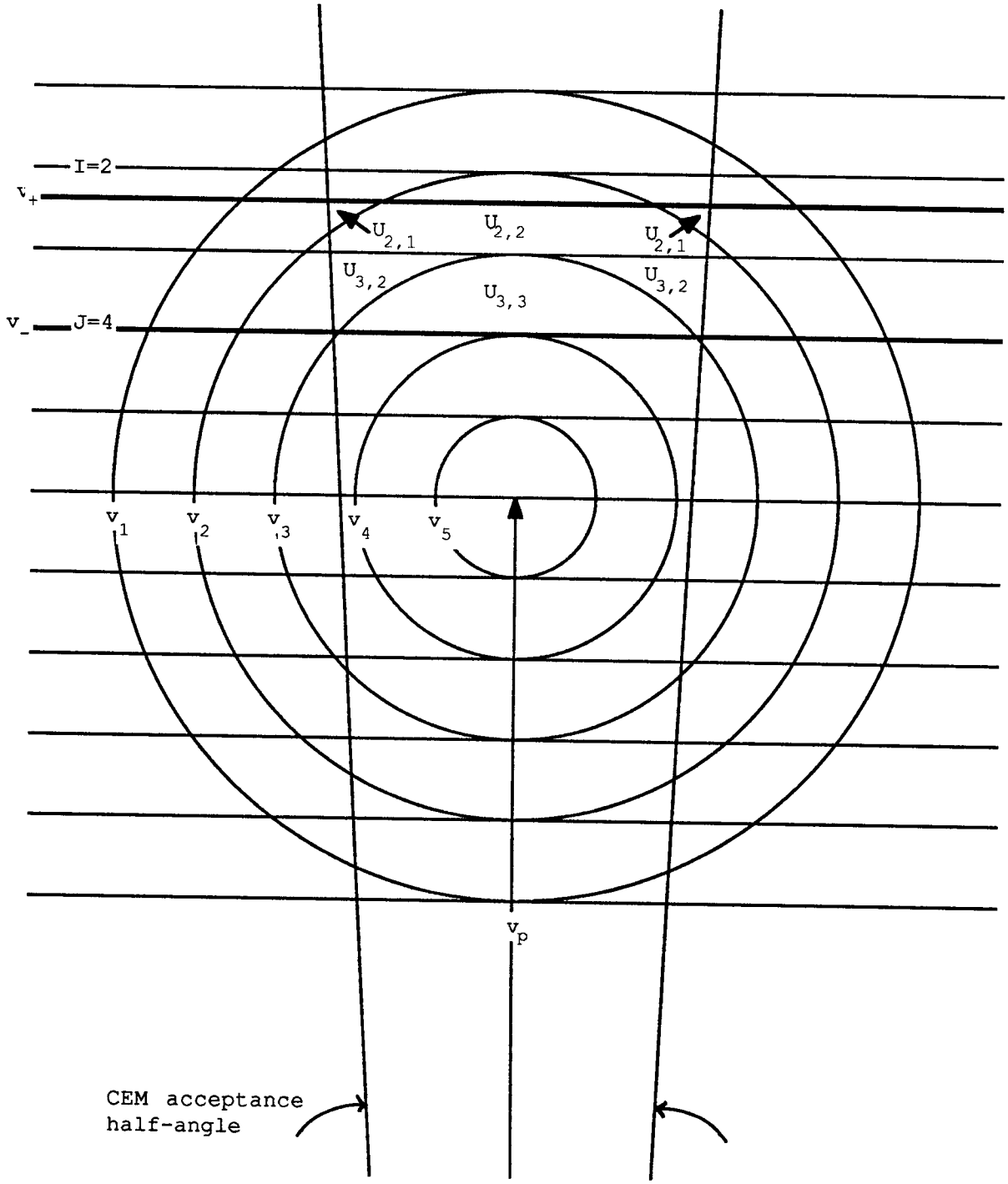

Figure 13. The partitioning of velocity space into shells and segments. $P(v)$ has a constant value, $P(v_j)$, in each shell of outer radius v_j and inner radius v_{j+1}.

this shell boundary is labeled by the index J, where J - 1 is equal to the index of the innermost shell in $(\delta v)^3$. Since δv may not be an

integral multiple of the step size between the radii, v_+ will not always lie on a shell boundary. The shell boundary with a radius greater than or equal to v_+ is labeled by the index I in figure 13. If v_+ is larger than v_h, I is given the value 1. The volume $(\delta v)^3$ is now sliced into segments by planes tangential to the shell boundaries and perpendicular to the beam direction. The fraction of the total volume of each spherical shell that lies within each segment is labeled $U_{j,i}$, where i is the fraction's shell index, and j is the index of the innermost shell in the segment. The value of $U_{j,i}$ is non-zero if some fraction of the ith shell lies in the segment of volume $(\delta v)^3$.

Using these definitions, the number of counts in the volume $(\delta v)^3$, which is the measured number of counts associated with the lab velocity $v' = v_p + v_{j+1} + \frac{\delta v}{2}$, is given by

$$(36)\quad N_{J-1} = \sum_{j=I}^{J-1} \sum_{i=1}^{j} T(v_i, \Omega_i)\, P(v_i)\, \frac{U_{j,i}}{U_i}\, \Delta v_i \ .$$

In other words, N_{J-1} is calculated by first summing products of the probabilities $P(v_i)\Delta v_i$ associated with each spherical shell which contributes to the segment, times the fractional volume of that shell within the segment, $\frac{U_{j,i}}{U_i}$, times the transmission function for that segment, $T(v_i, \Omega_i)$. The results are then summed over all segments within $(\delta v)^3$. In order to simplify the calculations, the transmission function is assumed to be rectangular, i.e. $T(v_i, \Omega_i)$ is assumed to be a constant, T, which is factored out of the summations. This is a reasonable approximation since the beam spot size is smaller than the entrance aperture of the analyzer, and the exit aperture is larger than the entrance aperture. According to the equations in table 2, the top

and bottom widths will be approximately equal. Equation 36 can now be solved for $P(v_K)$, where $K \equiv J - 1$, giving

$$(37)\quad P(v_K) = \frac{U_K}{U_{K,K}\,\Delta v_K}\left\{\frac{N_K}{T} - \left[\sum_{j=I}^{K-1}\sum_{i=1}^{j} P(v_i)\,\frac{U_{j,i}}{U_i}\,\Delta v_i + \sum_{i=1}^{K-1} P(v_i)\,\frac{U_{K,i}}{U_i}\,\Delta v_i\right]\right\}.$$

Equation 37 is the central equation for the deconvolution process.

The deconvolution of the data proceeds as follows: the number of velocity intervals between v" = 0 and v" = v_h is chosen. For v" > v_h, P(v) is assumed to be zero. In order to calculate $P(v_1)$, J is set to two, which makes $v_- = v_2$, and $v_+ > v_h$. $P(v_1)$ is calculated by multiplying N_2 by the ratio of the total volume of the outer shell to the volume $U_{1,1}$. After $P(v_1)$ is calculated, J is incremented and I is updated to reflect the current position of v_+. $P(v_2)$ is calculated from equation 37 now that $P(v_1)$ is known, and the process is repeated until all of the P(v)'s have been calculated. In figure 13, the deconvolution is at step 3, with J = 4 and I = 2. Volumes $U_{3,3}$ to $U_{2,1}$, $P(v_1)$ and $P(v_2)$ are used to calculate $P(v_3)$. The same procedure is repeated for the data from ions ejected in the backward direction. The value of J is first set to two, and all P(v)'s are calculated as before while J steps inward to the center. Once the P(v)'s have been calculated for the forward and backward directions, they are transformed to P(E)'s by the expression

$$(38)\quad P(E) = P(v)\frac{\Delta v}{\Delta E}\,.$$

Plots of P(E) vs the total CM energy E are shown in the following section.

The deconvolution procedure is tested by assuming that for 10 keV ArH^+, the dissociation cross section has a velocity dependence given by $P(v) \propto \frac{d\sigma}{dv} \propto \frac{1}{v^2}$. This form of the cross section in the CM frame implies $\sigma(v)$ = constant and $\sigma(E) \propto v^{-1}$. Equation 34 with a constant transmission function, T, is used to simulate a spectrum that would be measured for 10 keV ArH^+ dissociating with a dissociation cross section $\frac{d\sigma}{dv} \propto \frac{1}{v^2}$. From equation 34, the number of counts as a function of the analyzer voltage, N(v'), is

$$(39)\quad N(v') = \int_{\Delta v'} \int_{\Delta\Omega'} \frac{1}{v^2} T\, v'^2 dv' d\Omega'$$

With the substitution $v^2 = (v'^2 + v_p^2 - 2v'v_p\cos\theta)$, the integral can be evaluated, yielding

$$(40)\quad N(v') = A \frac{v'\Delta v'}{v_p} \left[\ln(v'^2 + v_p^2 - 2v'v_p\cos\theta) - 2\ln(v' - v_p) \right].$$

The velocity spectrum N(v') is deconvoluted as if it had been measured. Figure 14 contains a plot of the product of v and the calculated $\sigma(E)$ as a function of E. As figure 14 shows, the deconvolution yields the expected constant behavior, except for E values very close to E = 0. In this region, $\frac{d\sigma}{dv}$ diverges, and the finite step size in the deconvolution results in a deviation from a constant. If a large enough number of steps in v" are taken, the results of the deconvolution procedure become independent of the number of steps used. This test indicates that the procedure used to extract P(v) from the

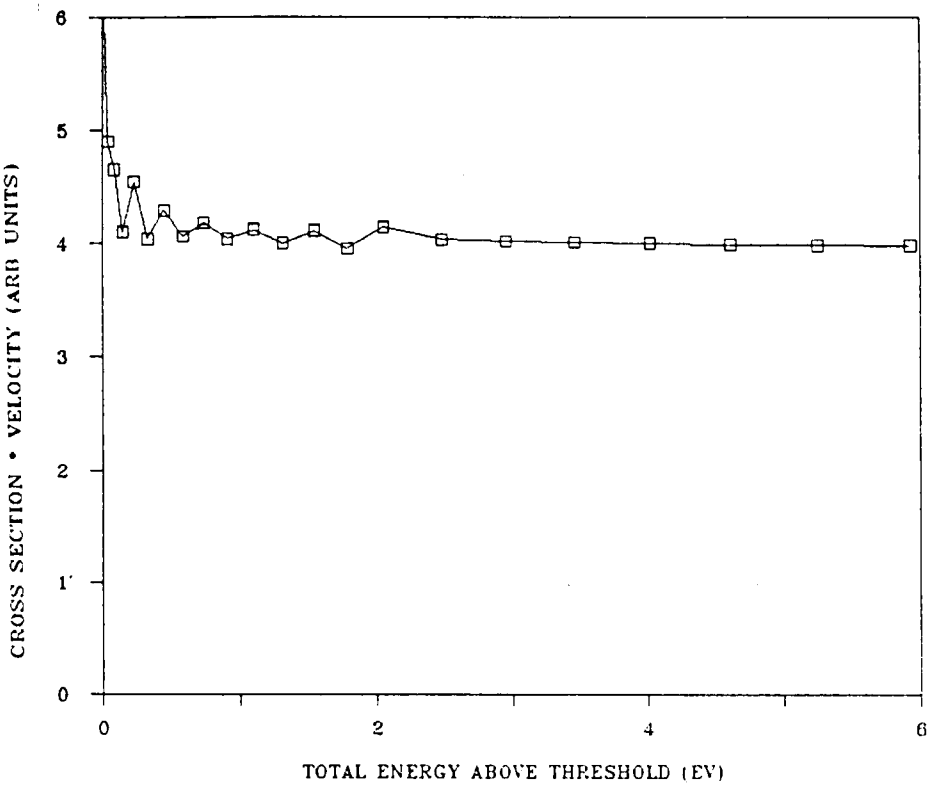

Figure 14. The product of v and $\sigma(E)$ vs E, where $\sigma(E)$ is calculated for $\frac{d\sigma}{dv} = \frac{1}{v^2}$.

coincidence data produces reasonable output for a predefined cross section. Therefore, the procedure is applied to the measured data with confidence.

C. Results

Energy spectra of protons resulting from the dissociation of ArH^+ are measured for 10 keV ArH^+ on He and Xe targets with acceptance angles of 0.025 and 0.036 rad, and for 20 keV ArH^+ on He and Xe targets with an acceptance angle of 0.036 rad. In figures 15 and 16, coincidence spectra measured in the laboratory frame and normalized to the same peak height are compared for the two targets and the two projectile energies.

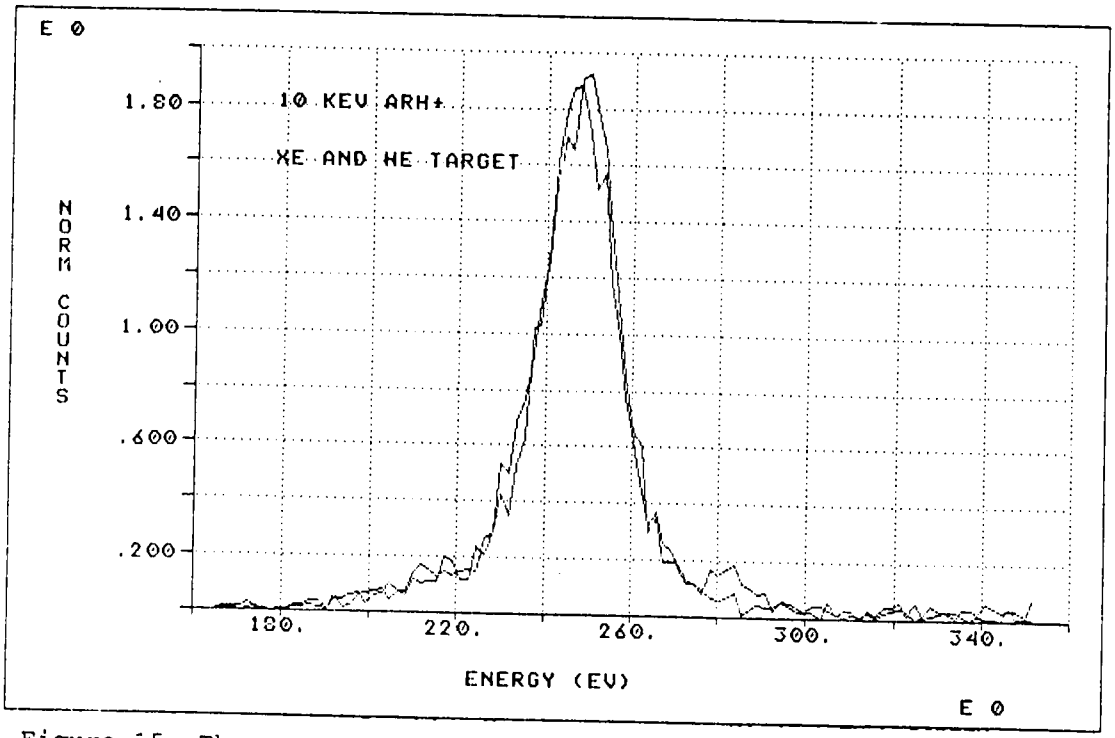

Figure 15. The energy spectra measured in the laboratory frame for 10 keV ArH^+ projectile impacting on He and Xe targets.

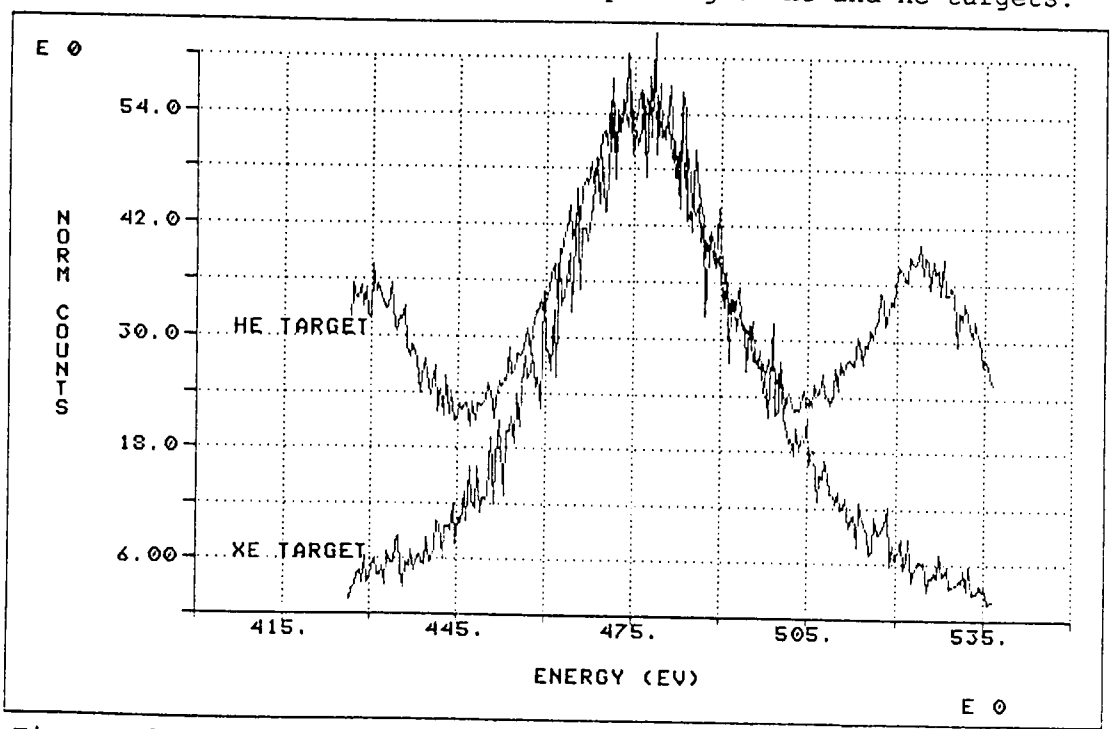

Figure 16. Energy spectra measured in the laboratory frame for 20 keV ArH^+ impacting on He and Xe targets.

For 10 keV ArH^+ projectiles, the spectra have identical shapes for the He and Xe targets within the scatter due to counting statistics. The dependence of the dissociation cross section on the total CM frame energy of the fragments is therefore independent of the target used, for 10 keV collision energies. The total fragment yield is approximately three times higher for a Xe target than for a He target. In the collision energy range from 10 to 20 keV, the cross section for vibrational dissociation of ArH^+ projectiles into a charged particle and a neutral with a total CM energy below 1 eV is found to be only weakly dependant on the collision energy. The value of the cross section is estimated from the measured data to be on the order of $10^{-19}cm^2$ for a He target. Since the detection efficiency of the detectors used in the present investigation is estimated and not measured, the exact absolute magnitude of the cross section is not determined.

The cross section for collisional dissociation due to electronic transitions depends strongly on the collision energy and target in the energy range of the present measurements. It is negligible compared to the cross section for vibrational dissociation for 10 keV ArH^+ projectiles impacting on both He and Xe targets and for 20 keV ArH^+ projectiles on Xe targets, but dominates the total dissociation cross section for 20 keV ArH^+ projectiles on He targets. Dissociation via electronic transitions results in fragments with well defined CM frame energies. In the energy spectra measured in the laboratory frame, these fragments form the characteristic side peaks observed above and below the central peak. This is shown in figure 16, where the spectra for 20 keV ArH^+ projectiles on He and Xe targets are overlayed. The energy and

angular resolution of the analyzer used in this investigation are not sufficient to allow the contributions due to electronic transitions to be uniquely separated from those due to vibrational transitions for the spectrum measured with 20 keV ArH^+ on He, so this spectrum is not analyzed further.

Figure 17 shows a plot of P(E) vs E for 10 keV ArH^+ on Xe with the results of the deconvolution for the forward and backward directions overlayed. The laboratory frame acceptance angle, θ_o, is 0.036 rad. The P(E) distributions in the forward and backward directions do not differ from each other more than different spectra taken with the same

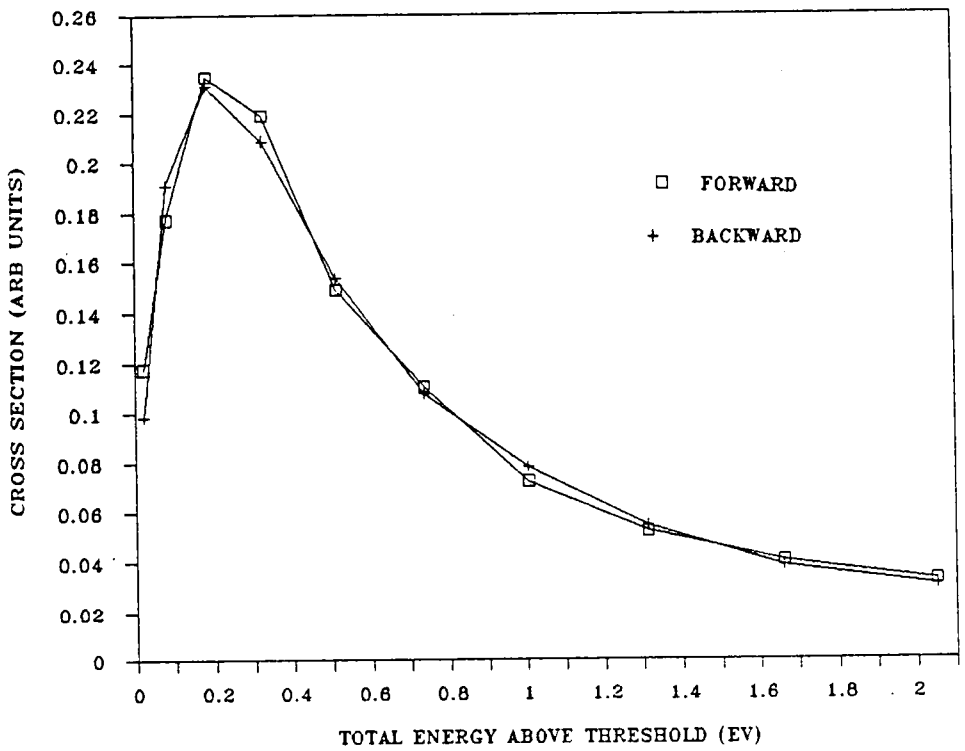

Figure 17. P(E), proportional to the dissociation cross section $\sigma(E)$, vs total CM energy E for 10 keV ArH^+ impacting on Xe. The results for fragments emitted in the forward and backward directions are overlayed.

parameters in the same direction differ from each other. The differences are dominated by counting statistics and uncertainties in the deconvolution process. The data therefore indicate that no forward-backward asymmetry exits.

Figure 18 shows a plot of P(E) vs E obtained from a spectrum measured for 10 keV ArH^+ projectiles impacting on He (θ_o = 0.036 rad) overlayed with the results obtained using a Xe target. When overlaying P(E) obtained from different spectra, the different distributions are normalized to equal areas under the lines connecting the six lowest energy data points. The probability distributions P(E) again do not significantly differ from each other, which is expected since the

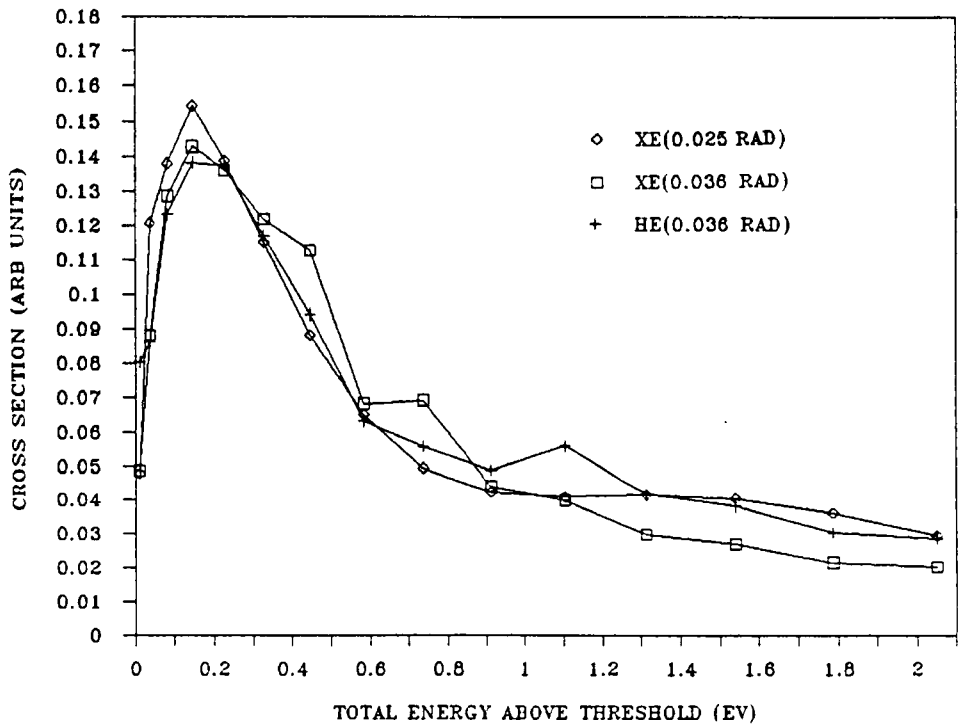

Figure 18. P(E), proportional to the dissociation cross section $\sigma(E)$, vs total CM energy E for 10 keV ArH^+ impacting on Xe and He targets with laboratory acceptance angles of 0.025 rad and 0.036 rad.

laboratory frame spectra have the same shape. Within experimental error, the energy dependence of the cross section, $\sigma(E) \alpha P(E)$, for ArH^+ striking He and Xe targets is independent of the target. Also shown in figure 18 is a plot of P(E) obtained from a spectrum measured in the laboratory frame with a smaller acceptance angle, $\theta_o = 0.025$. As can be seen in the figure, P(E) obtained from the deconvolution process described above is independent of the acceptance angle, which is consistent with the assumption of an isotropic $\frac{d\sigma}{dv}$. Overlaying plots of P(E) vs E obtained from laboratory frame spectra for 10 and 20 keV ArH^+ on Xe again indicates that no significant differences in the shape of P(E) exist (see figure 19). Therefore, the data taken in this investigation indicate that the energy dependence of $P(E) \alpha \sigma(E)$ is

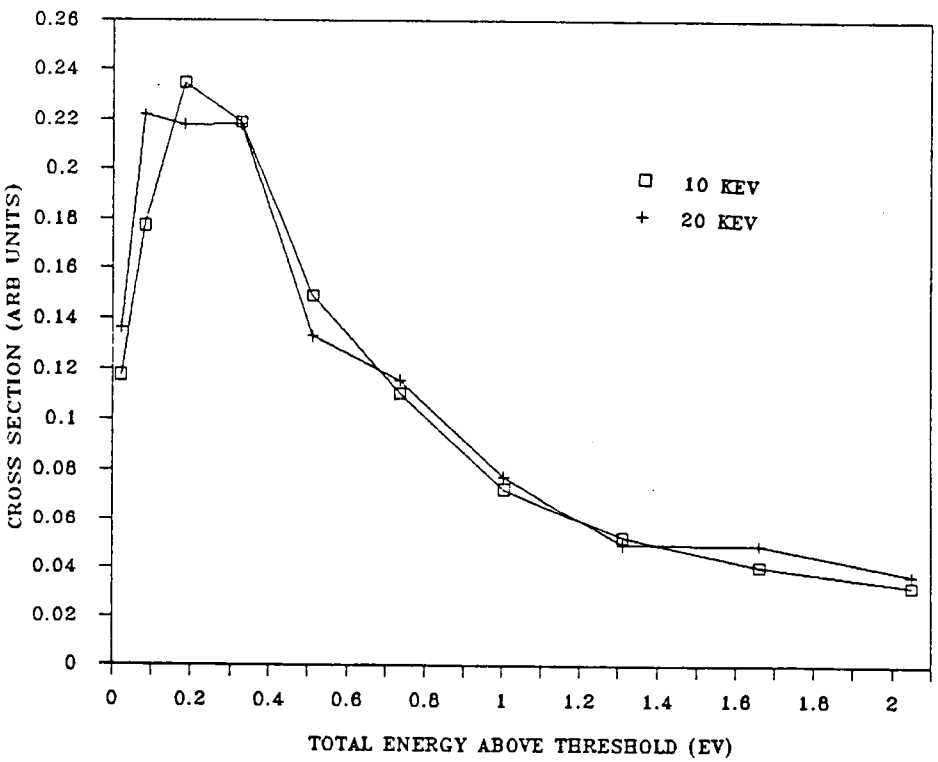

Figure 19. P(E) α σ(E) vs E for 10 and 20 keV ArH^+ impacting on a Xe target.

independent of the collision energy and target. P(E), which is proportional to the cross section for dissociation near threshold, is displayed in figure 20 for ArH^+ in fast collisions. The figure is obtained by averaging the results of all independent measurements with different collision energies and different targets. Errors due to counting statistics cannot be propagated through the deconvolution process. The error bars in figure 20 represent one standard deviation error from the averaging process. The step size used in the deconvolution process is varied when obtaining P(E) from different spectra. Figure 21 overlays P(E) derived using 30 steps with P(E) calculated using 20 steps in the deconvolution process. As long as

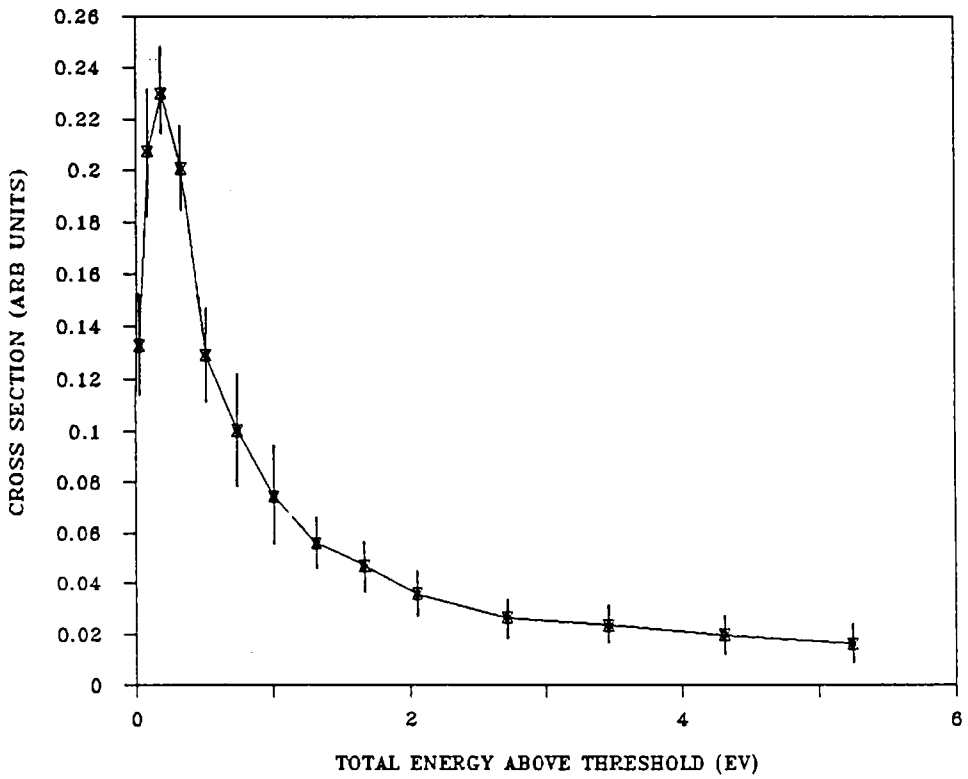

Figure 20. The average P(E) for ArH^+ averaged over the forward and backward directions and the He and Xe targets.

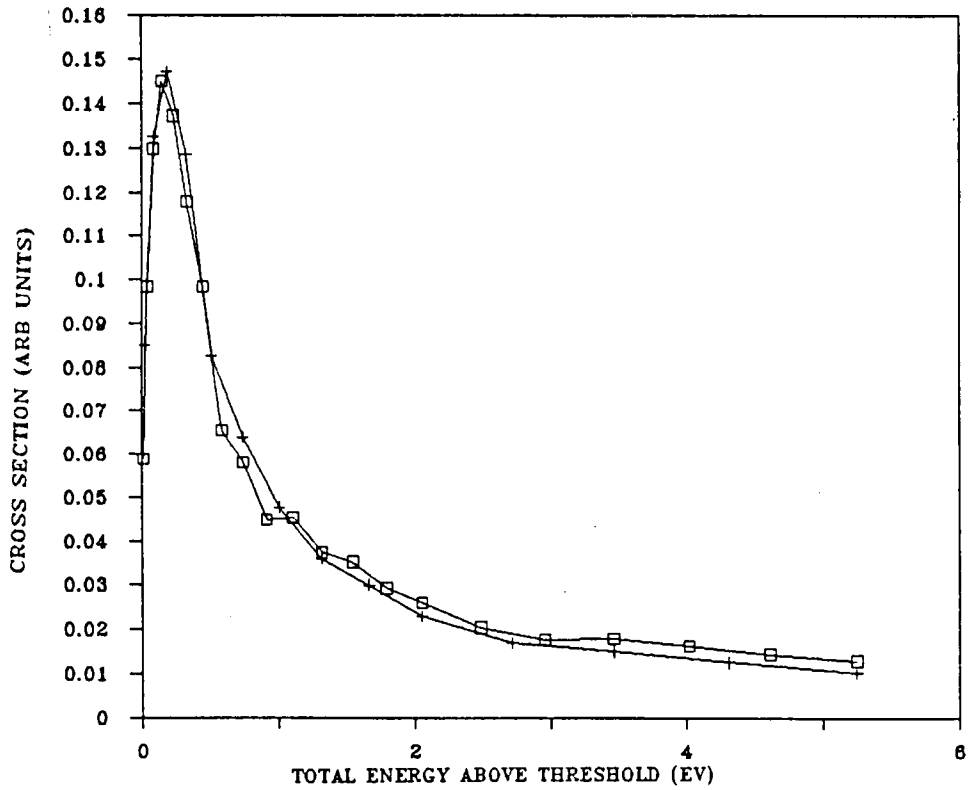

Figure 21. P(E) vs E obtained using 30 and 20 steps in the deconvolution process.

the step size is large enough, no systematic effects in P(E) are observed resulting from the varying step size.

Even though the deconvoluted data do not yield P(E) for E very near zero because of the finite step size used in the deconvolution process, the plots of P(E) vs E suggest that $\sigma(E)$ rises sharply near threshold. In the figures, however, P(E) approaches a maximum near E = 0.2 eV and drops to near zero as E increases.

The cross section for dissociation of N_2^+ into a singly charged ion, N^+, and a neutral N atom was measured for 6 keV N_2^+ projectiles on Xe and He targets. Two sets of measurements were made for both targets; one with an acceptance angle of 0.036 rad, and one with an acceptance angle of 0.025 rad. As for the ArH^+ projectiles, no differences beyond

those expected from experimental error and the uncertainties of the deconvolution process are observed in P(E) obtained from the different data sets. No forward-backward asymmetry is observed, and P(E) is independent of the laboratory acceptance angle used. The energy dependence of the dissociation cross section is the same for both targets. Since measurements are made at only one projectile energy, the dependence of the cross section on initial projectile energy cannot be tested. Figure 22 shows $P(E) \alpha \sigma(E)$ near threshold for N_2^+ projectiles dissociating in fast collisions. The results of all independent measurements are averaged, and the error bars represent one standard deviation error from the averaging process.

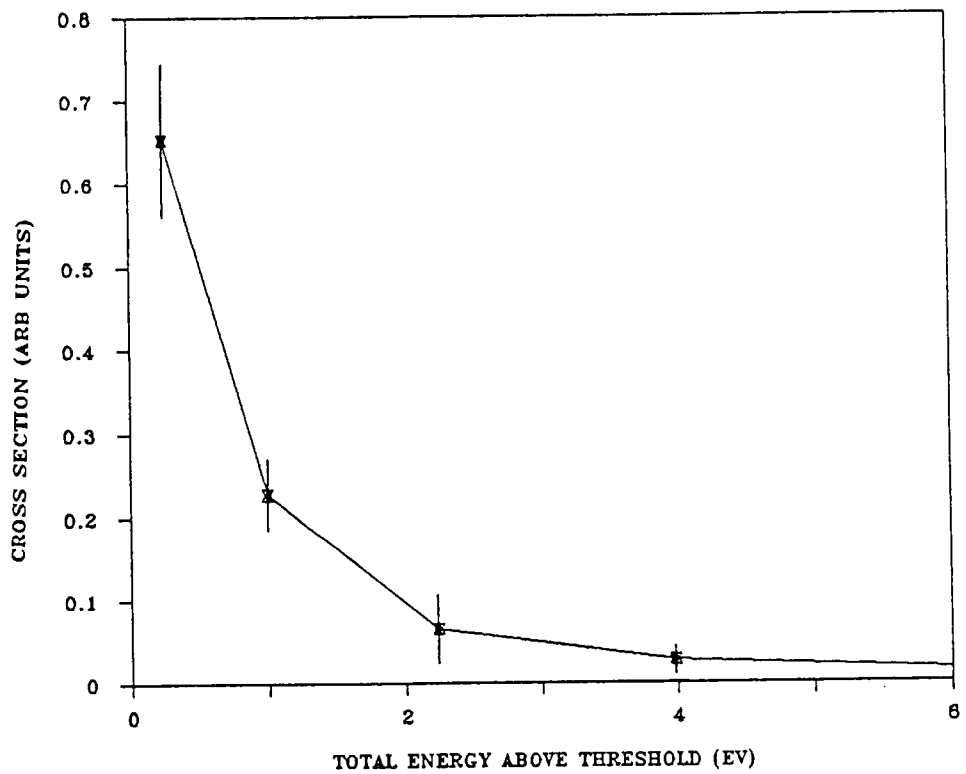

Figure 22. $P(E) \alpha \sigma(E)$ vs E for 6 keV N_2^+ projectiles.

The plot in figure 22 indicates that the dependence of the dissociation cross section on the total energy of the dissociation fragments above threshold for N_2^+ projectiles is similar to that of ArH^+ projectiles in fast collisions. In the case of for N_2^+ projectiles, however, P(E) cannot be evaluated for E close to zero. A N^+ ion has a large mass compared to the mass of a proton. Therefore, small Δv steps in the deconvolution process applied to the N_2^+ data correspond to energy steps ΔE that are much larger than the energy steps corresponding to equally small Δv steps in the deconvolution process applied to the H_2^+ and ArH+ data.

The cross section for dissociation of H_2^+ into a neutral H atom and a proton near threshold was measured for 6 keV H_2^+ projectiles on He and Xe targets with a laboratory acceptance angle of 0.025 rad. The deconvoluted data again indicate that $P(E) \alpha \sigma(E)$ is independent of the target, and that no forward-backward asymmetry exists. Figure 23 shows P(E) obtained by averaging all independent measurements made with H_2^+ projectiles. The plot again suggests that $\sigma(E)$ rises sharply very near threshold, reaching a maximum near 0.2 eV and dropping off to near zero as E increases. The peak in the distribution $\sigma(E)$ vs E is narrower for H_2^+ than for ArH^+.

In summary, the data yield a dissociation cross section $\sigma(E)$ near threshold that is consistent with the assumption of an isotropic $\frac{d\sigma}{dv}$. All of the data show $\sigma(E)$ to be independent of the target used in the collision, and of the laboratory acceptance angle used to take the data. The ArH^+ data further exhibit independence of the probability distribution on initial projectile energy. All data sets yield

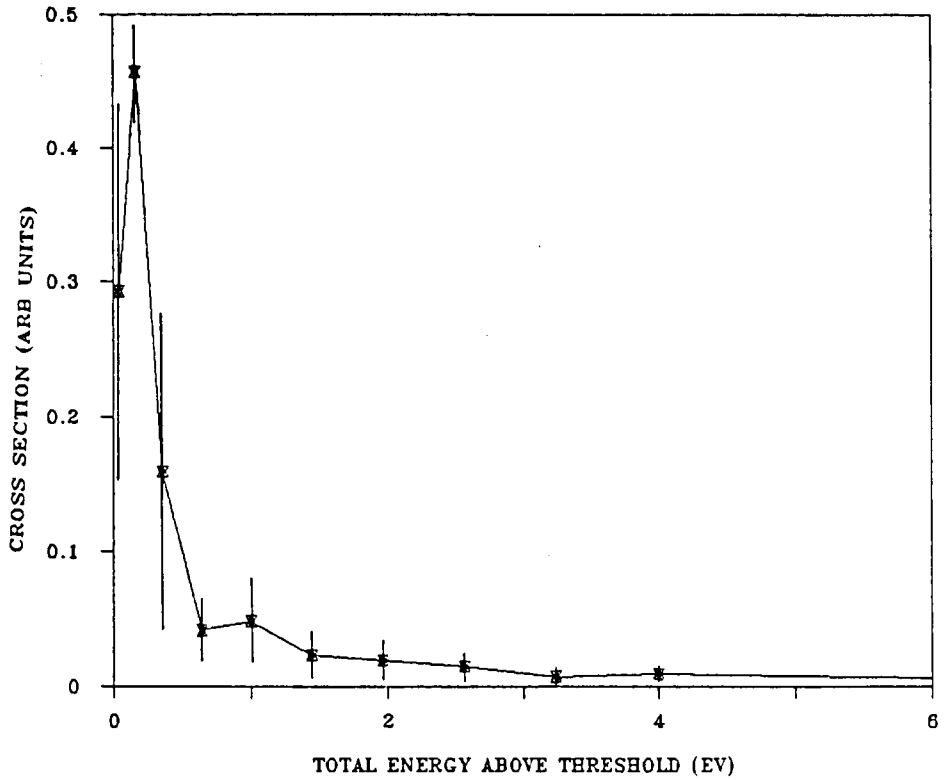

Figure 23. P(E) α σ(E) vs E for 6 keV H_2^+ projectiles.

σ(E) approaching zero for large values of the total CM energy, E, and a sharp rise in σ(E) as E decreases. The H_2^+ and ArH+ show a maximum in σ(E) near E = 0.2 eV and then a sharp drop-off for smaller E. P(0) cannot be obtained for any of the data sets because of the finite step size used in the deconvolution process.

D. Discussion

The results are interpreted as showing that the dissociation of diatomic molecules into a neutral atom and a singly charged ionic fragment with near zero kinetic energy in their center of mass frame in fast collisions with neutral noble gas targets can be described by a

two-body threshold law. The plots of P(E) vs E in figures 15 through 23 show that the energy dependence of the dissociation cross section is independent of initial projectile energy and of the target used. This behavior is consistent with the predictions of two-body threshold laws.

The final state of the dissociation fragments in the present investigation is that of two particles in a $\frac{1}{r4}$ polarization potential. For this potential, the energy dependence of the cross section should be dominated by the energy dependence of the normalization factor N(E) as long as $\sqrt{\frac{\beta}{k}}$ is smaller than the dimension of the initial bound state of the dissociating molecule, where β and k are defined in equation 28. For fragments with one eV total CM frame energy above threshold, $\sqrt{\frac{\beta}{k}}$ = 1.9 Å. Typical dimensions for the ground state of ArH^+, N_2^+, and H_2^+ are 1.28 Å, 1.12 Å, and 1.06 Å respectively.[10,21] Therefore, it is expected that a threshold law can describe the energy dependence of $\sigma(E)$ for $E < 1$ eV. The results of this investigation confirm this expectation. The exact form of $\sigma(E)$ cannot simply be calculated, however, since βk is large for 1 eV heavy particles, and expansions of N(E) made by assuming $\beta k \ll 1$ are not valid. However, the measured energy dependence of $\sigma(E)$ can be used to test future, more exact calculations of the normalization factor, N(E).

Another dissociation process which leaves the final state products in a polarization potential is detachment of electrons from negative ions. Itoh et. al.[22] have measured the energy spectra of electrons resulting from detachment collisions of H^- and D^- ions with rare gas atoms for collision energies between 2 and 250 eV. They did not transform their data to the projectile CM frame as was done here, but

they conclude that their data are in accordance with a kinematic model in which the H^- projectile acts as an emitter The shape of their measured spectra for small collision energies where a transformation to the CM frame will result in only small changes in the spectrum appears qualitatively similar to the shape of the spectra measured in this investigation (see figure 24).

Hotop et. al.[23] measured the photodetachment cross section of Au^-, Pt^-, PtN^-, and Ag^-. They found that the energy dependence of the photodetachment cross section only obeyed Wigner's law for the angular momentum barrier potential when the electron energy was below about 50 meV. At higher electron energies, terms arising from the polarization potential become increasingly important, and the threshold behavior of the cross section no longer obeys a simple $E^{l+1/2}$ rule of

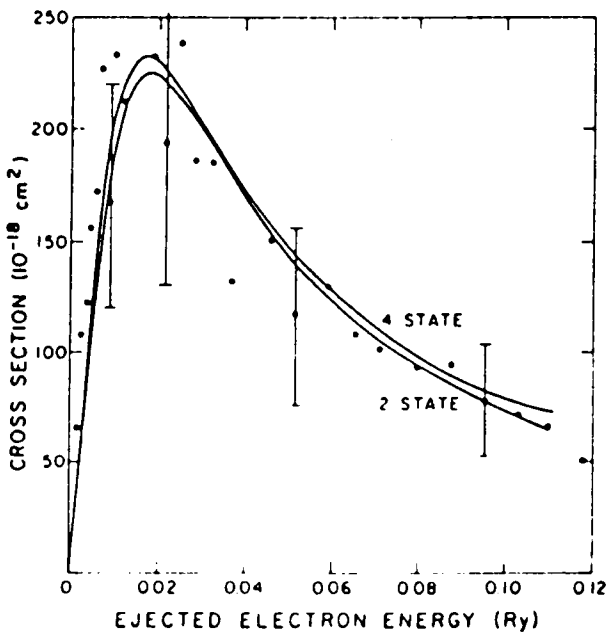

Figure 24. Detached electron energy spectra for collisional detachment of electrons from H^- on Kr at 25 eV.

Source: Y. Itoh, U. Hege, and F. Linder, J. Phys. B. **20**, 3437 (1987)

the angular momentum barrier potential. Similar measurements were made by Kaiser et. al.[24] for the photodetachment cross section of alkali negative ions over a wide photon energy range from .45eV to 2.5eV. The atom may be in an excited state after the photodetachment process. Excited states of alkali-metal atoms are highly polarizable, so the polarization potential becomes important in determining the energy dependence of the cross section for very low electron energies. Figure 25 shows the measured photodetachment cross section for K^- ions together with the results of ab initio multichannel calculations by Taylor and Norcross[25]. The calculation agree well with the measured data over a wide energy range. As in the case of the other negative ion detachment cross sections discussed, the general shape of the cross section as a function of energy is similar to the shape of the dissociation cross sections for diatomic molecules measured in this investigation.

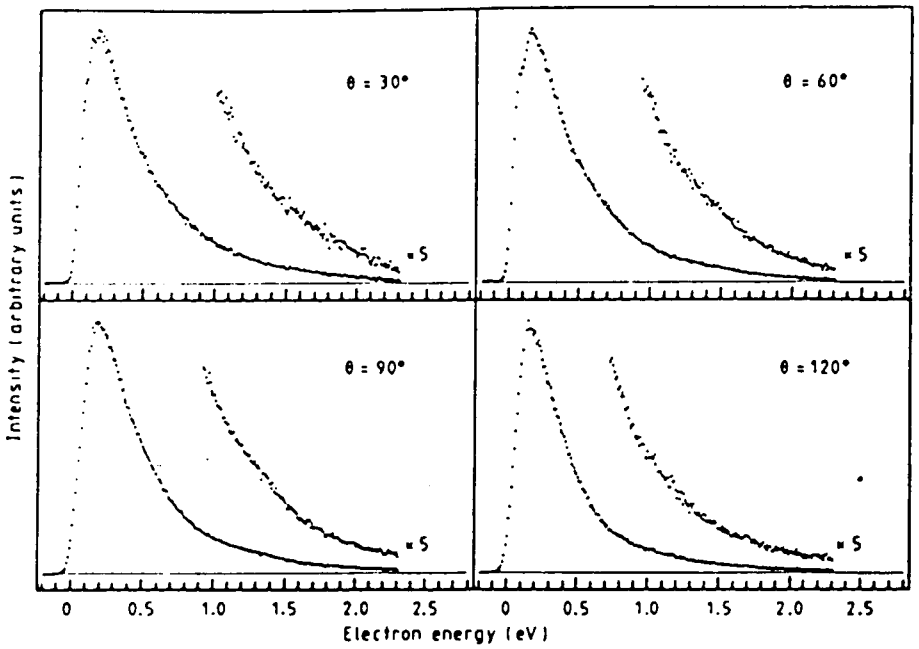

Figure 25. Total photodetachment cross section for K^-.

Source: K. T. Taylor and D. W. Norcross, Phys. Rev. A **34**, 3878 (1986).

In conclusion, this investigation shows that the dissociation of diatomic molecules after fast collisions with noble gas atoms into a singly charged ion and a neutral atom with low CM frame energy is a process that can be described by a two-body threshold law. Further, the energy dependence of the dissociation cross section is found to qualitatively agree with the energy dependence expected for a polarization potential. At the present time, no calculations exist which give the exact form of the cross section to be compared with the experimental results of this investigation, but the results may encourage future calculations of the energy dependence of the dissociation cross section near threshold.

Measuring the energy spectra of the dissociation fragments of a beam of molecular projectile ions provides a useful method for measuring the small CM frame energies of the dissociation fragments. The technique of measuring the energy spectra of the positive ionic fragments in coincidence with the neutral atoms allows the dissociation channel to be selected. Sacrifices made in this investigation in the energy resolution and the angular resolution of the analyzer used, are made in order to obtain sufficient counting statistics for the deconvolution process used to extract the cross section from the raw data. Future experiments of this nature can be made with better energy and angular resolution in order to refine the knowledge of the energy dependence of the dissociation cross section very near threshold.

List of References

List of References

1. Gordon W. McClure and James M. Peek, Dissociation in heavy particle collisions, (Wiley-Intersciences, New York 1972).

2. A.R.P. Rau, Threshold Laws in Atomic Physics, in Electronic and Atomic Collisions, Invited Papers of the XIII ICPEAC, edited by J. Eichler, I.V. Hertel, and N. Stolterfoht (North-Holland, Amsterdam, 1984), p. 711.

3. J. Los, Collision Induced Dissociation of Ions, Berichte der Bunsen-Gesellschaft für Physikalische Chemie, **77** , 640 (1973).

4. H. Ewald and W. Seibt, Collision Induced Dissociation of Diatomic Ions, in Recent Developments in Mass Spectroscopy, (University of Tokyo Press, Tokyo, 1970), p. 46.

5. J. Durup, Mechanisms of Collision-Induced Dissociation of Fast Ions, in Recent Developments in Mass Spectroscopy, (University of Tokyo Press, Tokyo, 1970), p. 921.

6. Frank L. Pilar, Elementary Quantum Chemistry, (McGraw-Hill, New York, 1968), p. 414.

7. David Park, Introduction to the Quantum Theory, Second Edition, (McGraw-Hill, New York, 1974), p. 498.

8. E. Cartmell and G.W.A. Fowles, Valency and Molecular Structure, Fourth Edition, (Butterworths, London, 1977), p. 53.

9. Claude Cohen-Tannoudji, Bernard Diu, and Frank Laloë, Quantum Mechanics, Volume I, (Wiley-Interscience, New York, 1977), p. 856.

10. Gerhard Herzberg, Molecular Spectra and Molecular Structure, I. Spectra of Diatomic Molecules, (Van Nostrand Reinhold, New York, 1950).

11. E.P. Wigner, Phys. Rev. **73**, 1002 (1948).

12. T.F. O'Malley, Phys. Rev. **137**, A1668 (1965).

13. T.F. O'Malley, L. Spruch, and L. Rosenberg, J. Math. Phys. **2**, 491 (1961).

14. H. Hotop, T.A. Patterson, and W.C. Lineberger, Phys. Rev. A **8**, 762 (1973).

15. S. Lasley, M. Breinig, Bull. Am. Phys. Soc. **31**, 929 (1986).

16. Jean Durup, Paul Fournier and Pham Dông, International Journal of Mass Spectroscopy and Ion Physics, **2**, 311 (1969).

17. P. Fournier, A. Pernot, and J. Durup, Journal De Physique **32**, 533 (1971)

18. A.G. Brenton, P.G. Fournier, B.L. Govers, E.G. Richard, and J.H. Beynon, Proceedings of the Royal Society of London A, **395**, 111 (1984).

19. F.W. Aston, Philosophical Magazine, **38**, 710 (1919).

20. K.D. Sevier, Low Energy Electron Spectrometry, (Wiley-Interscience, New York, 1972), p. 17, and references therein.

21. P. Rosmus, Theoret. Chim. Acta. **51**, 359 (1979).

22. Y. Itoh, U. Hege, and F. Linder, J. Phys. B. **20**, 3437 (1986).

23. H. Hotop and W. C. Lineberger, J. Chem. Phys. **58**, 2379 (1973).

24. H.J. Kaiser, E. Heonicke, R. Rackwitz, and D. Feldmann, Z. Physik **270**, 259 (1974).

25. K.T. Taylor and D.W. Norcross, Phys. Rev. A. **34**, 3878 (1986).

Vita

Scott Everett Lasley was born in Harriman, Tennessee on July 15, 1961. He moved to Louisiana in 1965, and graduated from Sunset High School in June, 1979. Scott received an Honor's Bachelor of Science degree in physics from the University of Southwestern Louisiana in June, 1983. He entered the University of Tennessee that summer and began study toward an advanced degree.

Scott received a Master of Science degree in physics in December, 1987 and obtained a position with the Space Physics Group at the University of Maryland.